Post-Print

This is the accepted version of:

M. Alioli, P. Masarati, M. Morandini, R. Albertani, T. Carpenter
Modeling Effects of Membrane Tension on Dynamic Stall for Thin Membrane Wings
Aerospace Science and Technology, Vol. 69, 2017, p. 419-431
doi:10.1016/j.ast.2017.07.008

Modeling effects of membrane tension on dynamic stall for thin membrane wings

Mattia Alioli[1], Pierangelo Masarati[2], Marco Morandini[3,*]

Politecnico di Milano, Dipartimento di Scienze e Tecnologie Aerospaziali, via La Masa 34, 20156, Milano, Italy

Roberto Albertani[4,*], Trenton Carpenter[5,*]

Oregon State University, Mechanical Engineering, 204 Rogers Hall Corvallis, 97330 OR

Abstract

An approach for predicting time varying aerodynamic loads on a pitching membrane wing due to rotational pitching and steady airflow is presented. The proposed model utilizes potential flow theory for a thin cambered airfoil with finite span, combined with a linearized representation of the membrane physics to predict lift under static conditions. Quasi-steady rotational effects and added mass effects are considered in a classic potential flow approach, modified for a membrane airfoil. A high-fidelity numerical model has been developed as well, coupling a viscous fluid solver and a non-linear membrane structural model, to predict the configuration of the system under static and unsteady loads. Moving Least Squares are used to map the structural and fluid interface kinematics and loads during the fluid-structure co-simulation. The static and dynamic lift predictions of the two models are compared to wind tunnel data, and show reasonable accuracy over a wide range of flow conditions, reduced frequency, and membrane pretension.

Keywords: dynamic stall; fluid-structure interaction; MAV; membrane wings;

Nomenclature

α	Angle of attack ($^\circ$)
α_o	Zero lift angle of attack ($^\circ$)
Æ	Wing aspect ratio
c	Normalized chord length
ϵ	Strain of the membrane
ε	Oswald efficiency
K_p	Potential flow lift constant
K_i	Induced drag constant
P	Pressure (N)
E	Modulus of elasticity (Pa)
ν	Membrane Poisson ratio
h	Membrane thickness (m)
λ	Membrane stretch ratio due to deformation
λ_o	Membrane stretch ratio due to pretension
ρ	Membrane material density (kg/m^3)
Re	Reynolds Number
U_∞	Free stream flow velocity (m/s)
k	Reduced frequency
X_{st}	Degree of trailing edge separation, static
$X(t)$	Degree of trailing edge separation, dynamic
$C_{L,st,dat}$	Coefficient of lift, static, wind tunnel data
$C_{L,d,dat}$	Coefficient of lift, dynamic, wind tunnel data
$C_{L,p}$	Coefficient of lift, static attached potential flow
$C_{L,v}$	Coefficient of lift, due to leading edge separation
$C_{L,mem}$	Coefficient of lift, due to membrane displacement
$C_{L,att}$	Coefficient of lift, total static attached flow
$C_{L,sep}$	Coefficient of lift, static separated flow
$C_{L,st}$	Coefficient of lift, static conditions
$C_{L,qs}$	Coefficient of lift, quasi-steady dynamic conditions
$C_{L,d}$	Coefficient of lift, dynamic conditions
$C_{L,fsi}$	Coefficient of lift, fluid-structure simulation

1. Introduction

Artificial micro flyers such as micro air vehicles (MAV) require highly agile maneuverability while maintaining benign flying characteristics in the entire flight envelope to prevent expanding the pilot or the autonomous flight control system beyond its capability. A significant body of early work on theoretical predictive models and experimental validation, including the fluid- structure interactions characterization, have elucidated the superior aerodynamic characteristics of flexible-wing MAVs, demonstrat-

*Corresponding author

Email addresses: mattia.alioli@polimi.it (Mattia Alioli), pierangelo.masarati@polimi.it (Pierangelo Masarati), marco.morandini@polimi.it (Marco Morandini), roberto.albertani@oregonstate.edu (Roberto Albertani), trenton.carpenter@gmail.com (Trenton Carpenter)

[1]Ph.D. & Research Assistant, Dipartimento di Scienze e Tecnologie Aerospaziali

[2]Professor, Dipartimento di Scienze e Tecnologie Aerospaziali

[3]Associate Professor, Dipartimento di Scienze e Tecnologie Aerospaziali

[4]Associate Professor, Mechanical Engineering

[5]Ph.D., Mechanical Engineering

ing the benign effects of a flexible wing with respect to a rigid configuration [1, 2, 3, 4] in steady flight conditions. A massive amount of work on flexible wings in unsteady conditions was performed by several authors on flapping wings in insects, birds and artificial wings in the last twenty years. A general view of aeroelastic implications on the aerodynamics of flapping wings was presented [5], as well as specific studies on effects of membrane wings on animal flight [6, 7] with specific applications on bats. Aeroelastic features on fixed wing configurations of flexible and membrane-wings in unsteady conditions have been presented including experimental studies [8, 9] and theoretical models [10]. Further research on fixed-wings MAV with membrane flexible wings was recently performed in unsteady conditions correlating membrane pretension levels, dynamic variation of wing pitching and angle of attack with the rotary-damping coefficients [11]. Specific research on wing membrane dynamics was also performed including vibrations [12, 13] and membrane pressrun a tailoring effects of wing performance [14, 15].

Dynamic stall of pitching airfoils includes a series of complex phenomena due to the delayed transient response of the fluid flow around the airfoil, cfr. [16, 17, 18, 19, 20, 21]. Rigid wings were experimentally investigated in wind tunnel tests used for validation of semi-empirical numerical models for transient post-stall aerodynamics for perching-flight mechanics studies [22]. Membrane-wings aerodynamics during dynamic stall conditions experimental results were performed presenting results on the correlation between membrane pretension, wing-pitch kinematics, Reynolds number and membrane shape at various reduced frequencies values [23]. In this work, a predictive lift model is presented for the dynamic stall phenomena of a dynamically pitching, perimeter reinforced, membrane wing. A combined analytic and empirical model is presented which utilizes existing and novel formulations of the dynamic aeroelastic phenomena surrounding the problem.

A membrane finite element formulation, implemented in a multibody formulation, cfr. [24], is used in co-simulation with a fluid dynamics solver to predict the configuration of the system under static and unsteady loads, as shown in [25, 26].

The experimental setup used in this work can accurately measure the full-field three-dimensional displacement and strain over a membrane wing in wind tunnel testing conditions. Digital Image Correlation (DIC) is used to measure strains and, in conjunction with a load cell, to estimate stresses and measure aerodynamic forces exerted on the membrane wing during wind tunnel testing. DIC measurements were used to generate virtual strain sensors on the surface of the membrane [27].

Analytical and numerical results, along with experimental measurements of actual membrane wing artifacts subjected to a variety of steady and unsteady flow conditions, are used to validate the proposed formulation.

2. Analytical Methods

The dynamic stall model presented in this work accounts for variation of lift due to a combination of leading edge separation, membrane deformation, and quasi-steady and transient delayed lifting effects from dynamic pitching. This model utilizes a state-space representation of the time varying, delayed stall effects due to dynamic motion [28]. For static angles of attack (AOA), loads generated by leading edge separation are modeled using a leading edge suction analogy for thin airfoils [29]. Moreover, the position of the trailing edge separation is estimated using wind tunnel test data to tune an empirical trailing edge separation model. The static contribution of lift from membrane deformation is modeled by applying several assumptions to the physics of the membrane. This method is detailed in Carpenter [30]; in the following section, a summary of this approach is discussed.

2.1. Static Lift Model

The static lifting curve, which is used as the "backbone" of the dynamic stall prediction, is generated by first defining two lift curves (under static AOA conditions); the first for fully attached flow, and the second for fully separated flow. Transition between these two states due to stall is determined using wind tunnel test data.

In this approach, the main contributions to lift of a thin membrane wing, for static AOA, are assumed to be from potential flow, leading edge separation, and cambering due to membrane displacement. The total lift under attached flow conditions[6] can thus be expressed, cfr. [30], as

$$C_{L,att} = C_{L,p} + C_{L,v} + C_{L,mem}. \tag{1}$$

In Eq. (1), $C_{L,p}$ is the lift coefficient for a finite length wing due to potential flow, i.e., $C_{L,p} = K_p(\alpha + \alpha_o)$, where α is the angle of attack (AOA), α_o is the AOA at zero lift ($C_{L,p} = 0$), and $K_p = \frac{2\pi}{\left(1+\frac{2\pi}{\pi\varepsilon \text{Æ}}\right)}$ is the potential flow constant, see e.g. [31][7]. Assuming that the flow reattaches past the leading edge separation bubble, the contribution to lift due to leading edge separation, $C_{L,v}$, for a rectangular wing can be written as $C_{L,v} = (K_p - K_p^2 K_i)\cos(\alpha)\sin^2(\alpha)$, where $K_i = \frac{1}{\pi\varepsilon \text{Æ}}$ is the induced drag constant [32]. Finally, $C_{L,mem}$ is the value of lift due to membrane displacement. To come to an expression for $C_{L,mem}$, it was assumed that the membrane displacement can be modeled as a circular arc, and the load applied to the membrane was an evenly distributed pressure. The membrane

[6] The term "attached" flow refers here to a flow which reattaches beyond the leading edge separation bubble and remains attached until the trailing edge.

[7] The contribution of lift due to unstable membrane displacement at zero AOA is accounted for in $C_{L,p}$, as shown in [30]. This model assumes the direction of unstable displacement to be in the direction of positive lift, thus generating a positive lift contribution, and does not consider the bifurcating effect which would occur if the wing was to sweep from a positive AOA to a large negative AOA.

is modeled as massless, linear elastic, constrained along all edges, with constant internal tension due to deformation and constant positive pretension in its reference configuration. Provided these assumptions, the state of membrane deformation can be equated to an aeroelastic coefficient, $Ae = \frac{Eh}{\frac{1}{2}\rho U_\infty^2 c} = \frac{Eh}{qc}$, where E is the linear modulus of elasticity of the membrane, h is the membrane thickness, ρ is the density of the fluid, U_∞ is the free stream velocity of the fluid, c is the wing chord, and q is the dynamic pressure. If the membrane out-of-plane displacement is assumed to fit the form of a circular arc, and the value of maximum displacement normalized to the chord length is defined as z, then it can be shown that: $\frac{C_L}{Ae} = f(\lambda_o, z)$, where f is a function to be determined and λ_o is defined as the stretch ratio due to pretension, i.e., $\lambda = (1 + \epsilon)$, where ϵ is the strain of the membrane due to deformation and/or pretension.

Using the potential flow solutions for a circular arc airfoil, a relationship between the AOA and membrane displacement (normalized to the chord), $z = z_{max}/c$, can be found for a finite aspect ratio rubber membrane wing:

$$\alpha + \sin^{-1}\left(2\eta \frac{Ae}{K_p}(\kappa - \lambda_o \phi)\right) - \frac{\phi}{4} = 0 \tag{2}$$

where ϕ and κ are the arc segment angle and radius of curvature respectively, as shown in Fig. 1, and $\eta = (1 + \frac{1}{\text{Æ}})$. For a chord length, c, equal to unity, ϕ and κ can be defined in terms of normalized max out-of-plane displacement, $z = z_{max}/c$, as:

$$\phi = 2\sin^{-1}\left(\frac{\kappa}{2}\right) \tag{3}$$

$$\kappa = \frac{8z}{4z^2 + 1}. \tag{4}$$

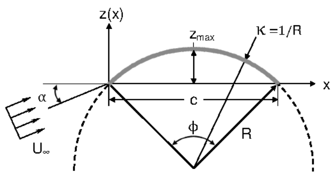

Figure 1: Geometry of a circular arc segment used to generalize the chordal shape of a displaced membrane airfoil.

Thus, given α, material properties and flow conditions, Eq. (2) can be used to find the value of camber z. Substituting z into Eq. (4), κ into Eq. (3), the value of lift due to membrane displacement for a finite aspect ratio wing can be defined as:

$$C_{L,mem} = K_p\left(\sin\left(\alpha + \frac{\phi}{4}\right) - \sin(\alpha)\right). \tag{5}$$

To model the lift coefficient of a separated flow, test data are considered for angles of attack beyond complete stall. Extending an empirical two dimensional lift model for separated flow (obtained considering wind tunnel test data [33]) to a finite aspect ratio wing, the lift coefficient for three dimensional separated flow can be approximated as

$$C_{L,sep} = \frac{\pi \sin(2\alpha)}{3 + \frac{1}{\varepsilon \text{Æ}}}. \tag{6}$$

Considering the attached flow model from Eq. (1) and the separated flow model from Eq. (6), a complete static lift model which transitions from fully attached to fully separated flow conditions can be defined. Let the degree of trailing edge separation be defined as $0 \leq X_{st} \leq 1$, where a value of $X_{st} = 1$ represents a condition of fully attached flow, and a value of $X_{st} = 0$ represents fully separated flow. Thus:

$$C_{L,st} = C_{L,att} X_{st} + C_{L,sep}(1 - X_{st}), \tag{7}$$

with

$$X_{st} = \frac{1}{\left[1 + \left[\left(\frac{\alpha}{\alpha^*}\right)^2\right]^{n_1}\right]^{n_2}} \tag{8}$$

The degree of separation model X_{st} used in this study is thus a blending function, so that the transition between the two models is smooth. For a given wing configuration and flow condition, the factors α^*, n_1, and n_2 are computed using wind tunnel test data. A least squares regression is used to minimize the error between lift data and the static AOA model, $C_{L,st}$.

2.2. Dynamic Stall Model

The dynamic stall model used in this work is a time varying, physics based model [28]. Quasi-steady rotational effects (i.e., circulation changes and boundary convection lag), which equate to instantaneous delayed lift and added mass loads, are considered using a potential flow approach for a thin airfoil. Considering a thin airfoil pitching about a quarter chord axis, and applying the thin airfoil theory, an effective AOA can be defined to account for quasi-steady rotational flow effects, viz., $\alpha_{qs} = \alpha + \frac{c}{2U_\infty}\dot{\alpha}$. Substituting this effective AOA into $C_{L,st}$ from Eq. (8), a model which describes quasi-steady dynamic lift is obtained as follows,

$$C_{L,qs} = C_{L,att}(\alpha_{qs}) X_{st}(\alpha_{qs}) + C_{L,sep}(\alpha_{qs})(1 - X_{st}(\alpha_{qs})) \tag{9}$$

A first order differential equation, which describes the transient/relaxation behavior of the separation point, is used to account for the delay (with respect to time) of the separation point in its progression along the airfoil, as AOA increases into stall regime, viz.

$$\tau_1 \dot{X}_d + X_d = X_{st}(\alpha - \tau_2 \dot{\alpha}) \tag{10}$$

where τ_1 is a dynamic separation point relaxation time constant. Coefficient τ_2 is a quasi-steady separation point time scaling constant, $\tau_2 = \tau_2^* \frac{c}{2U_\infty}$, where τ_2^* is a tuning parameter. Assuming a known kinematic pitching motion of the airfoil about the quarter chord position, where

$\hat{\alpha}_s$ and $\dot{\hat{\alpha}}_s$ are the known initial static AOA and pitch rate, Eq. 10 can be solved for $X_d(t)$ using a numeric ordinary differential equation solver and an initial condition of $X_d(t)|_{t=0} = X_{st}(\hat{\alpha}_s - \tau_2\dot{\hat{\alpha}}_s)$. $X_d(t)$ represents the dynamic separation point of the cambered airfoil due to a time varying pitching motion. With quasi-steady separation effects and transient separation effects modeled, a complete dynamic stall model is defined for a given pitching motion as,

$$C_{L,d} = C_{L,att}(\alpha_{qs})X_d(t) + C_{L,sep}(\alpha_{qs})(1 - X_d(t)) \quad (11)$$

3. Coupled Fluid-Structure Simulation

The overall approach adopted here was to use two different codes, i.e., a flow solver and a structural solver, and to exchange configuration and loads data between the two. This was achieved by adopting a tightly coupled fluid-structure co-simulation, in which the structural problem is solved using the free general-purpose multibody dynamics solver MBDyn[8], developed at Politecnico di Milano [34], and the fluid problem is solved using a dedicated solver based on FEniCS[9] [35, pp. 171-222]. With few high-level Python statements, FEniCS supports the definition of the discretized weak form of complex systems of Partial Differential Equations (PDEs), and can drive the solution of the ensuing nonlinear problem. The FEniCS Form Compiler (FFC) automatically generates the low-level C++ code that efficiently computes the residual vector and its Jacobian matrix for the problem at hand. A tight coupling, i.e. the exchange between the viscous flow and the structural solver of configuration and loads data at each iteration until mutual convergence was found necessary, due to the strong interaction of the fluid and the membrane structure in this problem. The computational analyses are assessed with experimental results. Specifically, we highlight our ongoing efforts geared towards developing an integrated computational and experimental approach to perform aeroelastic analyses of membrane wings within various configurations.

Structural Solver. A four-node isoparametric membrane element, based on second Piola-Kirchhoff type membranal resultants, is implemented in MBDyn for the analyses in this work [24]. The membranal stresses are computed as functions of their work-conjugated Green-Lagrange strains. The classical Enhanced Assumed Strains (EAS) method [36] is exploited to improve the response of the element; seven additional variables for each membrane element are added to the strain vector [37].

Fluid Solver. The fluid dynamics code is based on a stabilized finite element approximation of the unsteady Navier-Stokes equations, often referred to in the literature as General Galerkin, or G2, method [38]. The so-called ALE cG(1)cG(1) formulation, with friction boundary conditions [38, 39], was chosen. In short, G2 is a weighted least-squares stabilized Galerkin finite element method in space-time. The stabilization of G2 acts as an automatic turbulence model in the form of a generalized artificial viscosity model acting selectively on the smallest scales of the mesh [40]. In particular, the stabilized cG(1)cG(1) method is a type of G2 method with continuous piecewise linear *trial* functions both in time and space, for both velocity and pressure, and continuous piecewise linear *test* functions in space and piecewise constant *test* functions in time.

Aeroelastic Coupling. The coupling of viscous flow and structural solvers used in this work requires the definition of a common interface. In particular, the multibody solver is coupled with the external fluid dynamics code by means of a general-purpose, meshless boundary interfacing approach based on Moving Least Squares with Radial Basis Function [41]. This is accomplished by precomputing a linear interpolation operator, $\mathcal{H}$, that computes the interface aerodynamic nodes displacement $\mathbf{x}_a$ from the structural nodes displacements: $\mathbf{x}_a = \mathcal{H}\,\mathbf{x}_s$. To guarantee the conservation of the (virtual) work done in the two domains, the linear operator that computes the aerodynamic forces applied to the structural nodes, $\mathbf{f}_s^a$, is the transpose of the interpolation matrix $\mathcal{H}$, viz.: $\mathbf{f}_s^a = \mathcal{H}^\top \mathbf{f}_a^a$. The computer implementation of the ALE technique requires the formulation of a mesh-update procedure that assigns mesh-node velocities and displacements at each time step. The mesh deformation process moves the fluid mesh nodes according to a linear elastic "fictitious" problem, where the elastic modulus of each element is proportional to the inverse of its volume. If the volume of an element becomes negative as a consequence of the displacement of the interface nodes, the elastic modulus of such an element is increased and the linear elastic problem is solved again.

4. Modeling

Aerodynamic tests were performed in a low speed wind tunnel. Lift and membrane displacement for a wing pitching with static and dynamic AOA were measured. Measured data were compared with predictions from the two previously discussed methods. Tests were conducted on wing models with varying membrane pretension, subject to various flow conditions and pitching rates. The test matrix was built by varying the membrane pretension (λ_o), the flow velocity (U_∞), the pitch rate ($\dot{\alpha}$), the reduced frequency (k), and the starting pitch angle (α_{st}). The pitching amplitude (α_{amp}) was held constant at 10° peak-to-peak, and the pitching axis was held constant at 25% chord position throughout the tests.

4.1. Wind Tunnel Testing

The test article used in the wind tunnel is a 2:1 aspect ratio, rectangular, perimeter reinforced membrane wing.

[8] http://www.mbdyn.org/.
[9] http://fenicsproject.org/.

The wing, which has a span of 280 mm and chord of 140 mm, is made with two shaped steel frames ($E = 210$ GPa, $\nu = 0.3$, $\rho = 7800$ kg/m^3, with a frame width and thickness of 5 mm and 1 mm, respectively). A rubber latex membrane ($E = 1.14$ MPa, $\nu = 0.4$ and $\rho = 960$ kg/m^3), held at a prescribed in-plane pretension, was sandwiched between the two steel frames. Images of the actual test article can be seen in Fig. 2, and a schematic of the test set-up is illustrated in Fig. 3.

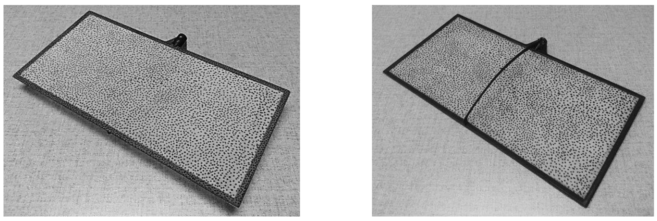

(a) Top View (b) Bottom View

Figure 2: 2:1 membrane wing, with steel perimeter and speckled rubber latex membrane.

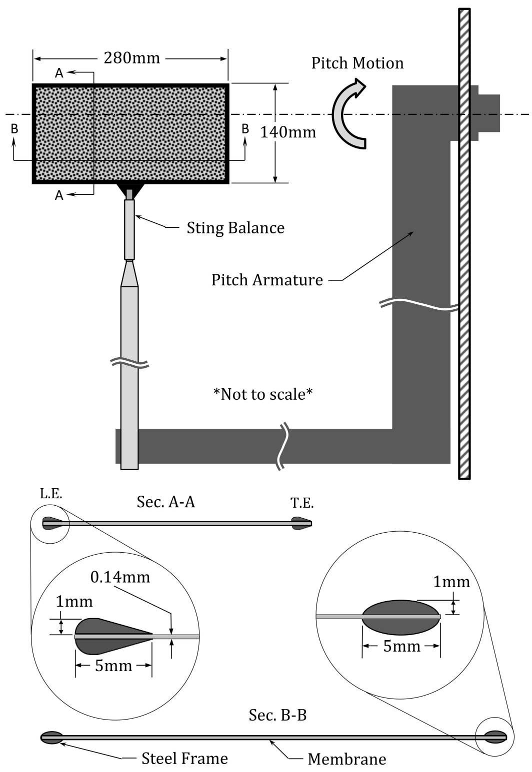

Figure 3: Wind tunnel pitching fixture and membrane wing with frame geometry.

A range of flow conditions with Reynolds number between 50k–100k were tested. Reduced frequency values of $k = \{0, 0.05, 0.1\}$ were used while operating within the pitching motor's operational envelope. Three target cambers were selected using Waldman's membrane displacement approach [42], resulting in three membrane wings with corresponding stretch ratio of $\lambda = \{1.02, 1.058, 1.085\}$. In addition to these stretch ratios, a relatively high value of λ was also tested in order to see the influence of the frame on the aerodynamics of the wing, compared to the frame plus a compliant airfoil. The test matrix is summarized in Fig. 4. In that figure, each line represents a

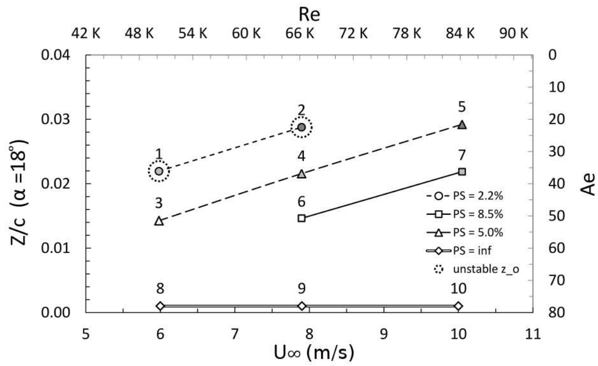

Figure 4: Predictions of membrane camber for different test conditions.

membrane wing model with different pretension (PS), each point represents a test condition (with a label corresponding to each unique test condition), and the points circled with a dotted line represent conditions of unstable membrane displacement at zero AOA. In addition to testing the four membrane configurations ($\lambda = \{1.02, 1.058, 1.085\}$ and $\lambda \to \infty$), a 2:1 flat plate was also tested to serve as a basis of comparison to a well known aerodynamic profile. The geometry of this 2:1 flat plate wing conformed to the leading edge, trailing edge and thickness dimensions defined by Mueller [43]. This flat plate ("Mueller" from now on) was tested for static AOA conditions and all dynamic AOA conditions. For each condition in Fig. 4, data were collected at static AOA, for $\alpha = -2°$ to $30°$, at $2°$ increments. For all wing configurations, dynamic sweeps were performed using $\alpha_{st} = \{0°, 5°, 10°\}$, $\alpha_{amp} = 10°$, and $k = \{0.05, 0.1\}$. Finally, a commonly accepted Oswald efficiency factor for rectangular wings of $\varepsilon = 0.9$ [44] for all wings within the study is applied.

The low-speed closed loop wind tunnel is capable of speeds from 1 to 18 m/s and has a 1.3×1.5 m test section. Aerodynamic loads from the wing were measured by a six degree-of-freedom sting balance fixed directly at the trailing edge. The system was capable of simultaneously pitching, measuring aerodynamic loads and performing non-intrusive displacement measurements via DIC. Load and angle channels were recorded at 500 Hz, and DIC images were taken at 500 frames per second[10]. Time varying data from the load cell were averaged to identify a measurement of the steady state coefficient of lift and drag for each test condition.

[10]DIC measurements were averaged over the 500 snapshots which were taken at 500 Hz for a duration of 1 second.

4.2. Numerical Modeling

The structural grid, implemented within the multibody simulation environment provided by MBDyn, consists of 8×16 four-node membrane elements, involving 153 structural nodes. To model the steel frame surrounding the membrane wing, 24 three-node beam elements were added to the structural model. The mass lumped in each node is computed from the latex rubber sheet portion associated with the node, which is uniformly distributed, and in addition, for the boundary nodes, from the portion of the steel frame associated with the node [26].

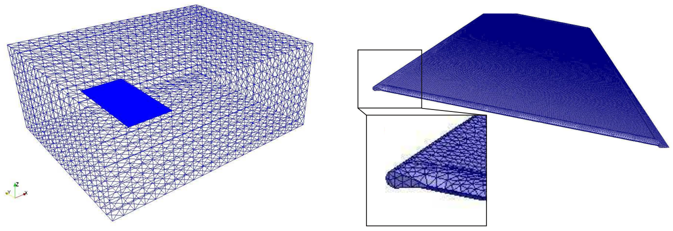

(a) CFD simulation domain. (b) Meshed membrane wing.

Figure 5: CFD domain.

The fluid simulation volume, shown in Fig. 5, consists of approximately 270k nodes and 1.4 million tetrahedrons with a cell width of 0.2 mm in the near wake region, and cells growing up to 10 mm near the simulation boundaries. At the domain inlet the velocity magnitude and direction are set as boundary conditions, while at the outlet a constant pressure is specified. The other four boundary walls are characterized by a slip wall boundary condition. A "skin friction model" was used to simulate slip with (linear) friction and penetration with resistance boundary conditions on the wing surface [38, 39]. This choice does not allow to completely resolve the boundary layer; it brings, however, substantial computational savings without completely compromising the simulation accuracy. The leading and trailing edge are modeled as flexible, aerodynamically shaped supports, as shown in Fig. 5(b).

5. Results

To evaluate the ability of the proposed approaches of estimating dynamic lift due to pitching, experimental wind tunnel loads and membrane displacements are compared to the proposed models under varying conditions of flow velocity, pretension, pitching frequency, and AOA pitching ranges. In Section 5.1, the contributions to the static lift curve resulting from the analytical model (i.e., $C_{L,p}$, $C_{L,v}$, $C_{L,mem}$, $C_{L,att}$, $C_{L,sep}$, and X_{st}), are compared with time averaged, static test data, $C_{L,st,dat}$, and with the results from the coupled fluid-structure analysis, $C_{L,fsi}$. In Section 5.2, dynamic (analytical) lift predictions, $C_{L,qs}$, and $C_{L,d}$, are compared with dynamic test data as functions of α and time for varying dynamic pitching conditions.

5.1. Non-Pitching Case

Fig. 6(a) shows the coefficient of lift with respect to AOA for the 2:1 "Mueller" flat plate, with a thickness of 3.2 mm. Thus, for this wing, the leading edge separation is minimal, i.e., $C_{L,v}(\alpha) = 0$. Since the wing is stiff, we assume $C_{L,mem} \approx 0$. Thus, $C_{L,p} = C_{L,att}$, meaning the calculation of potential flow should adequately model the flat plate for pre-stall AOA. Observing Fig. 6(a), it is noticed that for $\alpha < 12°$, the potential flow component of lift accurately predicts measured lift. For high AOA, wind tunnel data approaches $C_{L,sep}$ asymptotically as expected. Using data, $C_{L,att}$, and $C_{L,sep}$, a regression fit is used to generate X_{st}, from which $C_{L,st}$ can be calculated.

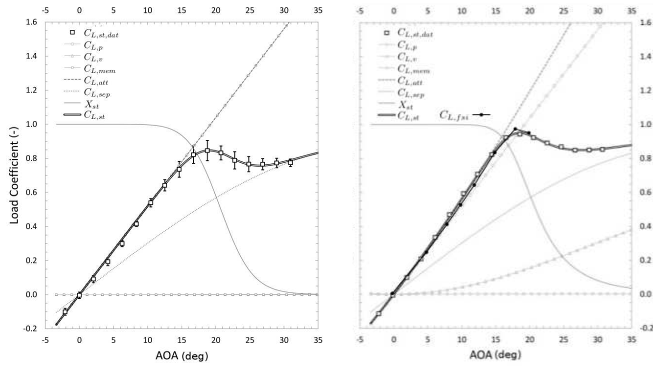

(a) 2:1 "Mueller" flat plate. (b) Wing with "rigid" membrane.

Figure 6: Static lift model and wind tunnel data. (a) 2:1 "Mueller" flat plate, (b) membrane wing with "rigid" membrane.

The error bars in Fig. 6(a) represent 95% confidence intervals; in most cases they are smaller in magnitude than the square points representing the measurement in the figure. To reduce figure complexity, confidence intervals will not be presented on further graphs.

Fig. 6(b) shows the results obtained with the perimeter reinforced membrane wing, where the membrane is replaced with a thin "rigid" plate of comparable thickness. For this wing, leading edge separation is expected so that $C_{L,v}(\alpha) \neq 0$, while $C_{L,mem}$ is still driven to zero, thus $C_{L,att} > C_{L,p}$. As previously noted, $C_{L,att}$ accurately models lift for low angles of attack, and the data appears to converge toward $C_{L,sep}$ for large AOA, although slower than in the previous case. The lift coefficient predicted by the coupled fluid-structure analysis, $C_{L,fsi}$, is also shown in Fig. 6(b). It should be noted that for these rigid wings, $C_{L,st}$ are invariant to changes in flow velocity within the ranges of this study ($Re = 50\text{k}-84\text{k}$).

The analytical and numerical models show good agreement with the experiments, for lift over the rigid wing prior to stall. In general, results from Fig. 6 confirm that both models have the capability to accurately predict lift over a large range of static AOA, for the 2:1 rigid flat plate and for the 2:1 membrane wing with a rigid membrane, experiencing leading edge separation. Compliant membranes are considered next.

The predicted max camber, $z(\alpha)$, is compared with DIC measurements. Fig. 7 represents the (average) maximum measured and predicted static camber, z_{dic} and z_{st} respectively, for a flow velocity of $U_\infty = 8$ m/s ($Re = 66$k), and prestretch $\lambda_o = 1.058$ (or 5.8% average prestrain). The max camber, computed by the coupled fluid-structure simulation, z_{fsi}, is also reported for comparison.

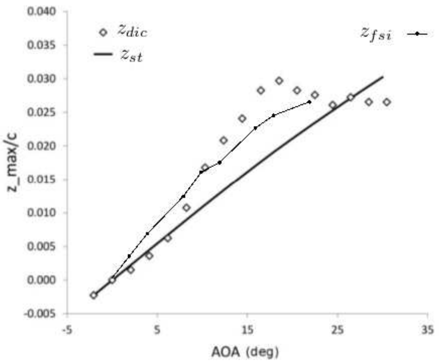

Figure 7: DIC and predicted displacement.

The analytical predicted maximum camber fairly accurately models measured displacements up to about $\alpha = 8°$. Given the linearizing assumptions built into the prediction model for membrane displacements and loads, the resulting analytical model represents the physics of the system for small AOA. The abrupt change in the experimental displacement at $\alpha = 8°$ indicates that there is an interaction mode that is not captured in the analytical model. Given the analytical results of the membrane camber predictions presented above, it is expected that the estimated coefficient of lift will be slightly underpredicted for intermediate AOA, $\alpha = 8°$ to $18°$. The numerical predicted max camber z_{fsi}, instead, better reproduces measured displacements from $\alpha = 10$ deg. For α below this value, the numerical prediction is slightly over-estimated. Correlation between both models and experiments is nevertheless deemed acceptable, with the numerical model slightly over-predicting the local membrane inflation for small AoAs.

Fig. 8(a) shows lift coefficient versus AOA for test condition "3" in Fig. 4, $\lambda_o = 1.058$, $U_\infty = 6$ m/s ($Re = 50$k), while Fig. 8(b) depicts test condition "4" in Fig. 4, $\lambda_o = 1.058$, $U_\infty = 8$ m/s ($Re = 66$k). Attached lift slope and peak lift are greater for the higher velocity case. This is due to the increased contribution of $C_{L,mem}$ and to the difference in dynamic pressure, as illustrated in Fig. 8. Both test conditions show a stable membrane at zero AOA, i.e., zero camber and thus zero lift at zero AOA, both for the experiment and the numerical simulations. The static lift curve $C_{L,fsi}$ as given by the coupled fluid-structure analysis is also shown in Fig. 8(b) for comparison.

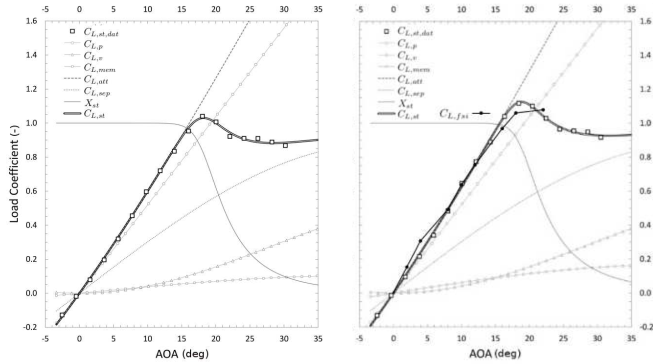

(a) 5.8% prestrain, $Re = 50$k. (b) 5.8% prestrain, $Re = 66$k.

Figure 8: Static lift model, perimeter reinforced membrane wing.

5.1.1. *Effect on Flexible Wing*

The lift and drag coefficients were computed, both for the experimental wind tunnel test and the fluid-structure simulation, by averaging their values over time. However, in some conditions the actual response is not stationary. Fig. 9 reports the time evolution of the numerical (high-fidelity) aeroelastic system for two different values of AoA, $\alpha = 8$ and 12 deg, respectively, starting at non-dimensional time $t^* = t\frac{V}{c} = 4$ to $t^* = 20$. Similar non stationary behavior of the wing membrane out of plane displacement and modal characteristics have been observed and reported in previous theoretical [45, 46] and experimental [47, 48, 49, 50, 9] research work. The evolution of the normalized aerodynamic coefficients C_L and C_D, and the membrane maximum amplitude, w, is shown. The values are normalized with respect to their maximum value.

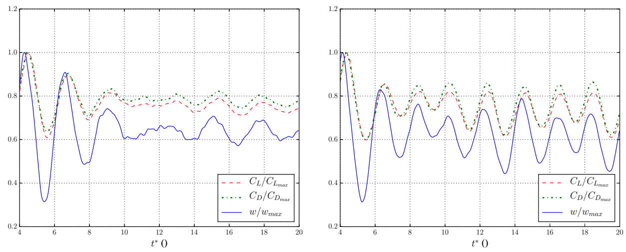

(a) $\alpha = 8$ deg. (b) $\alpha = 12$ deg.

Figure 9: Flexible membrane at 5.8% prestrain, $Re = 66$k. Mid-membrane point displacement and global C_L–C_D histories.

As depicted in Fig. 9, the maximum value of deformation came after about $t^* \approx 5$, and reaches a "steady" value after about $t^* = 20$ chords for the membrane at $\alpha = 8$ deg, while for $\alpha = 12$ deg the oscillation continue beyond $t^* = 20$.

Fig. 10 shows the deformation contour at different times t^*, for the membrane at 5.8% prestrain, $U_\infty = 8$ m/s and $\alpha = 8$ deg.

The primary wing deformation mode is an inflation that increases the local camber. A Proper Orthogonal De-

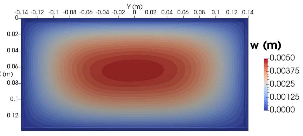

(a) $t^* = 4$.

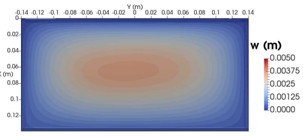

(b) $t^* = 10$.

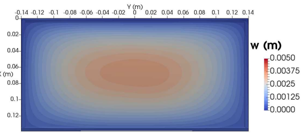

(c) $t^* = 16$.

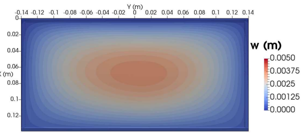

(d) $t^* = 20$.

Figure 10: Deformation contours for $U_\infty = 8$ m/s, $\alpha = 8$ deg, membrane at 5.8% prestrain.

composition (POD) of the membrane deformation, for the problem with $U_\infty = 8$ m/s, $\alpha = 8$ deg, with the membrane at 5.8% prestrain, shows that the main modes excited are the first four. They comprised about 85% of the original system energy, see Fig. 11(a) and Fig. 11(b).

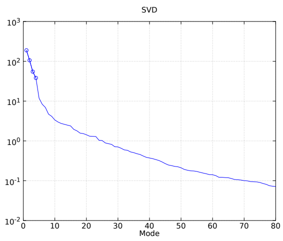

(a) SVD.

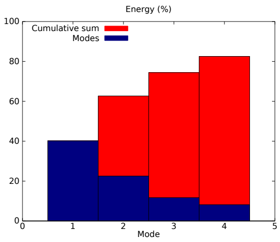

(b) Energy content.

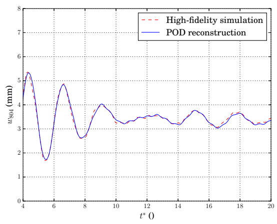

(c) POD reconstruction.

Figure 11: POD results for the flexible membrane at 5.8% prestrain, $U_\infty = 8$ m/s, $\alpha = 8$ deg.

The first four Proper Orthogonal Modes (POMs) are shown in Fig. 12.

In order to limit the amount of data that has to be post-processed for model reduction and allow a preliminary assessment of the potentials of the POD for the aeroelastic problem of flexible membrane wings, only the structural degrees of freedom were considered in the POD. The coordinates of all the membrane points at every time step of the numerical simulation are used to build the snapshot matrix, $\mathbf{S}$, whose columns contain the values of the system variables at each time step. Afterwards, $\mathbf{S}$ is used

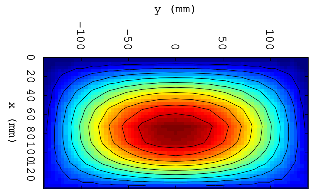

(a) POM 1.

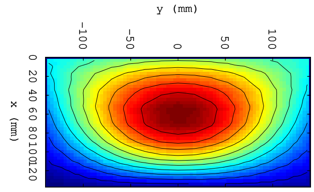

(b) POM 2.

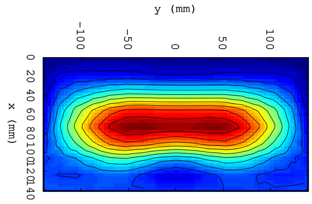

(c) POM 3.

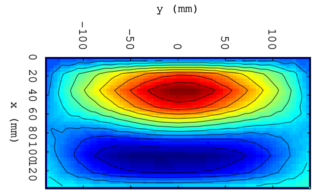

(d) POM 4.

Figure 12: First four POMs, $U_\infty = 8$ m/s, $\alpha = 8$ deg, membrane at 5.8% prestrain.

for the calculation of the correlation matrix, $\mathbf{C} = \mathbf{S}^\top\mathbf{S}$. The eigenvectors of $\mathbf{C}$ define the basis of the projection matrix that can be used to project the time history of the state variables and obtain the time evolution of the amplitude of each base considered [51]. The amplitudes are the new variables of the reduced-order system; their number depends on the number of retained eigenvectors of $\mathbf{C}$. Fig. 11(c) compares the displacement history of the central point of the membrane from the high-fidelity simulation and the POD reconstruction of the same time history with the 4 selected modes, and shows that the first four basis functions capture the displacement history well.

5.1.2. *Effect on Flow Structure*

Having established sufficient confidence in the aeroelastic membrane wing model, attention is now turned to the computed flow structures. No experimental validation is available for this work. Fig. 13 shows the predicted pressure contours by the coupled fluid-structure simulation on the upper and the lower wing surface. The pressure dis-

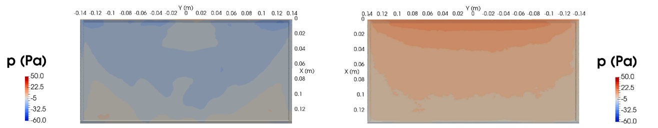

(a) Rigid wing.

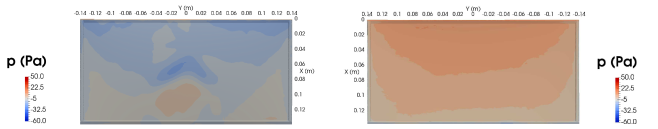

(b) Membrane at 5.8% prestrain.

Figure 13: Pressure contours on the wing surface (Left: top, Right: bottom), $U_\infty = 8$ m/s, $\alpha = 8$ deg, $t^* = 50$.

tributions at 8 deg angle of attack, $U_\infty = 8$ m/s, for the upper surface of the rigid and flexible wing at 5.8% prestrain, are given in Fig. 13 (left). For the rigid wing, a high pressure region is located close to the leading edge, corresponding to flow stagnation. This is followed by pressure recovery (minimum pressure), and by a mild adverse pressure gradient, which is strong enough to cause the flow to separate. For the flexible membrane wing, the inflated membrane shape pushes the bulk of the flow separation closer to the leading edge. On the underside of the rigid wing, Fig. 13 (right), the pressure gradient is largely favorable, smoothly accelerating the flow from leading to trailing edge. Load alleviation on the lower surface of the flexible membrane wing is evident by a decrease in the high-pressure regions associated with camber, and a growth of the suction region at the trailing edge, presumably due to a decrease in the local incidence.

The pressure difference between the lower, high-pressure zone and the upper, low-pressure zone induces a spanwise flow that bends the streamlines towards the wingtips and accelerates the flow near the tips. The tip vortex can be

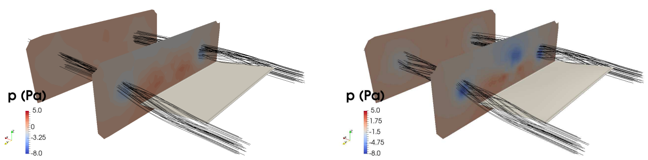

(a) Rigid wing. (b) Membrane at 5.8% prestrain.

Figure 14: Pressure contours and streamlines in the wake behind the wing, $U_\infty = 8$ m/s, $\alpha = 8$ deg, $t^* = 50$; the cross-section planes are 0.5 c and 1.5 c behind the trailing edge.

easily observed from the streamline structure. In Fig. 14 the pressure contours behind the rigid and the membrane wing at 5.8% prestrain are plotted, for $R_e = 66$k, at $t^* = 50$. The low-pressure zone observed in the planes perpendicular to the flight direction characterizes the vortex core.

The effect of camber on flow structure is shown by the vorticity contours of Fig. 15, plotted at $t^* = 50$. The

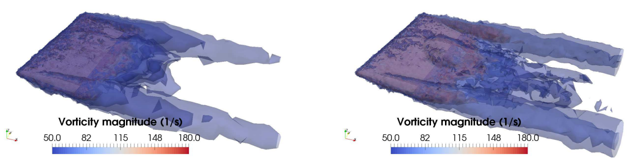

(a) Rigid wing. (b) Membrane at 5.8% prestrain.

Figure 15: Isosurface of vorticity, $U_\infty = 8$ m/s, $\alpha = 8$ deg, $t^* = 50$.

strongest wake vortices are located near the wing tips, showing that the circulation gradient is largest there. Flow visualization suggests that the wing deformation contributes to stronger wing tip vortices.

5.2. Pitching Case

As demonstrated in previous results, both the unsteady numerical and the analytical static lift model adequately represent the lift behavior for the rigid and membrane wings within the study. This is important, since the (analytical) dynamic stall model is based on the static one, adding terms that account for pitch rates and time variant separation. Wings were tested under different flow velocities, $U_\infty = \{6, 8, 10\}$ m/s (i.e., $Re = \{50\text{k}, 66\text{k}, 84\text{k}\}$), two reduced frequencies, $k = \{0.05, 0.1\}$, and three AOA ranges, $\hat{\alpha} = \{0° \text{ to } 10°,\ 5° \text{ to } 10°,\ 10° \text{ to } 20°\}$. The em-

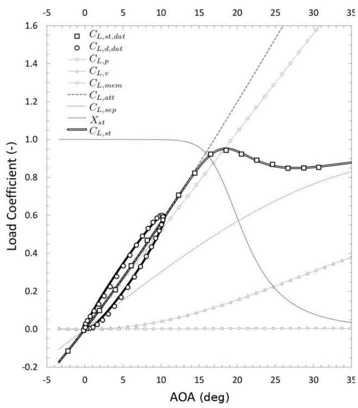

Figure 16: Dynamic lift model for rigid membrane, pitching at $k = 0.05$ for $\alpha_s = 0°$ and $\alpha_{amp} = 10°$, flow velocity of 8 m/s ($Re = 66k$).

pirical time constant τ_2^* was tuned using dynamic wind tunnel data, cfr. [30], under low AOA pitching maneuvers[11]. Considering a single sinusoidal oscillation $\hat{\alpha} = \{0° \text{ to } 10°\}$, at a reduced frequency of $k = 0.05$, with a flow velocity of $U_\infty = 8\ m/s$ ($Re = 66$k), a value of $\tau_2^* = 4$ was found to produced accurate dynamic lift predictions, as a function of α, as shown in Fig. 16. All subsequent results were computed with the same value of τ_2^*.

Next, τ_1 was tuned using data from a high AOA sweep. Fig. 17 shows the same wing, with same flow conditions and pitch rate, but for a motion where $\hat{\alpha} = \{10° \text{ to } 20°\}$. In this case, a value of $\tau_1 = 8.5$, produced accurate predictions with respect to AOA. This value of τ_1 was used for all the other predictions.

With the established values for τ_1 and τ_2^*, all membrane wings subjected to all testing conditions could be modeled and compared to measured values. Dynamic stall prediction for various membrane pretensions and flow velocities are reported in Fig. 18, 19, and 20. The results produced by this predictive model appear to be fairly robust to changes in flow velocity, pitching frequency, AOA ranges, and membrane tensions.

[11] For pitching maneuvers at low AOA, or where $X_{st}(\alpha) = 1$, the rate of trailing edge separation $\dot{X}_{st} = 0$, i.e., there is no separation at low AOA. Thus, results are time invariant and are directly proportional to $\dot{\alpha}$, and $C_{L,d}$ is invariant to changes made to τ_1.

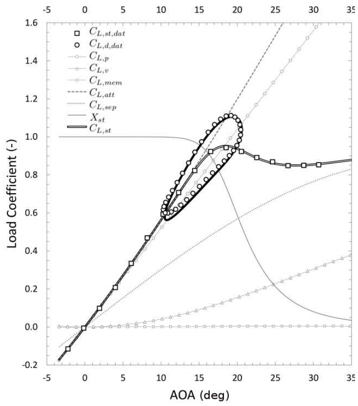

Figure 17: Dynamic lift model for rigid membrane, pitching at $k = 0.05$ for $\alpha_s = 10°$ and $\alpha_{amp} = 10°$, flow velocity of 8 m/s ($Re = 66k$).

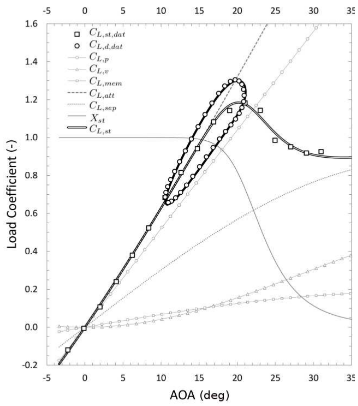

Figure 18: Dynamic lift model for a membrane at 8.5% prestrain, pitching at $k = 0.05$ for $\alpha_s = 10°$ and $\alpha_{amp} = 10°$, flow velocity of 10 m/s ($Re = 84k$).

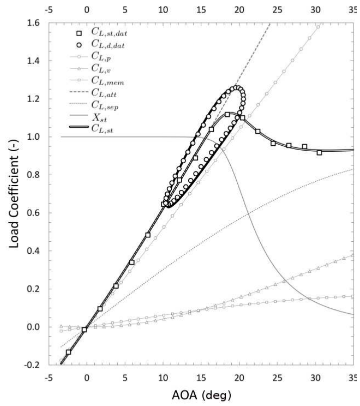

Figure 19: Dynamic lift model for a membrane at 5.8% prestrain, pitching at $k = 0.05$ for $\alpha_s = 10°$ and $\alpha_{amp} = 10°$, flow velocity of 8 m/s ($Re = 66k$).

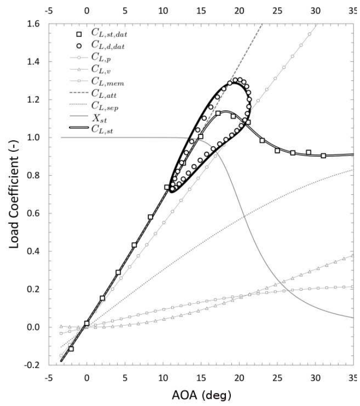

Figure 20: Dynamic lift model for a membrane at 2.0% prestrain, pitching at $k = 0.05$ for $\alpha_s = 10°$ and $\alpha_{amp} = 10°$, flow velocity of 6 m/s ($Re = 50k$).

6. Summary & Conclusion

A dynamic stall model is presented in this paper utilizing potential flow estimations of lift for static conditions to generate a static AOA lift model for attached and separated flow. Test data was used to predict the location of trailing edge separation for a given test scenario in order to produce an accurate static lift model for low to high AOA. This model incorporates a prediction of lift due to static leading edge flow separation and membrane cambering. The stability criteria for membrane cambering at zero AOA was identified, and the magnitude of unstable cambering was predicted with acceptable accuracy for the conditions tested. With a complete static lift model, dynamic variations of lift were included due to instantaneous flow recirculation effects, added mass effects, and transient flow separation. A first order, state space representation was used to model the time varying delayed separation effect experienced at high AOA. Over a wide variety of flow conditions, pitching rates, AOA ranges, and membrane pretensions, the proposed analytical model produced acceptably accurate results.

A four-node membrane element was implemented in a multibody-based co-simulation analysis for the direct simulation of coupled fluid-structure problems. As shown in the results, the numerical model accurately predicts attached flow conditions and trailing edge separation. Thus, it adequately represents the lift behavior for the membrane wings within this study. A methodology was also introduced for the reduced order modeling of the membrane wing based on proper orthogonal decomposition. POD projection allowed the definition of a very low order model that can capture the main features of the system, demonstrating the suitability of a reduction approach based only on structural information for the reduced-order modeling of this class of aeroelastic systems.

This approach favorably correlated to data and could be well suited for real-time load estimation, given known airspeed and AOA. The concept of "feeling flight" is a simple one, yet the practical implementation and analytic formulation of this is not quite as straight forward. All told, this body of work has covered an array of load estimation approaches intended to further the understanding of the aerodynamics of membrane wings.

Acknowledgments

Effort sponsored by the Air Force Office of Scientific Research, Air Force Material Command, USAF, under grant number FA8655-12-1-2114, technical monitor Dr. Gregg Abate. The U.S. Government is authorized to reproduce and distribute reprints for Governmental purpose notwithstanding any copyright notation thereon.

[1] Y. Lian, W. Shyy, Three-Dimensional Fluid-Structure Interactions of a Membrane Wing for Micro Air Vehicle Applications, in: 44th AIAA/ASME/ASCE/AHS/ASC Structures, Structural Dynamics, and Materials Conference, American Institute of Aeronautics and Astronautics, 2003, dOI: 10.2514/6.2003-1726.
URL https://arc.aiaa.org/doi/abs/10.2514/6.2003-1726

[2] P. Ifju, M. Waszak, L. Jenkins, Stability and control properties of an aeroelastic fixed wing micro aerial vehicle, in: AIAA Atmospheric Flight Mechanics Conference and Exhibit, American Institute of Aeronautics and Astronautics, 2001, dOI: 10.2514/6.2001-4005.
URL https://arc.aiaa.org/doi/abs/10.2514/6.2001-4005

[3] R. Albertani, B. Stanford, J. P. Hubner, P. G. Ifju, Aerodynamic Coefficients and Deformation Measurements on Flexible Micro Air Vehicle Wings, Experimental Mechanics 47 (5) (2007) 625–635. doi:10.1007/s11340-006-9025-5.
URL https://link.springer.com/article/10.1007/s11340-006-9025-5

[4] R. Albertani, B. Stanford, J. Hubner, P. Ifju, Characterization of Flexible Wing MAVs: Aeroelastic and Propulsion Effects on Flying Qualities, in: AIAA Atmospheric Flight Mechanics Conference and Exhibit, American Institute of Aeronautics and Astronautics, 2005, dOI: 10.2514/6.2005-6324.
URL https://arc.aiaa.org/doi/abs/10.2514/6.2005-6324

[5] W. Shyy, H. Aono, S. K. Chimakurthi, P. Trizila, C.-K. Kang, C. E. S. Cesnik, H. Liu, Recent progress in flapping wing aerodynamics and aeroelasticity, Progress in Aerospace Sciences 46 (7) (2010) 284–327, doi:10.1016/j.paerosci.2010.01.001.

[6] A. Song, X. Tian, E. Israeli, R. Galvao, K. Bishop, S. Swartz, K. Breuer, Aeromechanics of Membrane Wings with Implications for Animal Flight, AIAA Journal 46 (8) (2008) 2096–2106. doi:10.2514/1.36694.
URL https://doi.org/10.2514/1.36694

[7] R. Waldman, A. Song, D. Riskin, S. Swartz, K. Breuer, Aerodynamic Behavior of Compliant Membranes as Related to Bat Flight, in: 38th Fluid Dynamics Conference and Exhibit, American Institute of Aeronautics and Astronautics, 2008, dOI: 10.2514/6.2008-3716.
URL https://arc.aiaa.org/doi/abs/10.2514/6.2008-3716

[8] P. Rojratsirikul, Z. Wang, I. Gursul, Unsteady Aerodynamics of Low Aspect Ratio Membrane Wings, in: 48th AIAA Aerospace Sciences Meeting Including the New Horizons Forum and Aerospace Exposition, American Institute of Aeronautics and Astronautics, 2010, dOI: 10.2514/6.2010-729.
URL https://arc.aiaa.org/doi/abs/10.2514/6.2010-729

[9] I. Gursul, D. J. Cleaver, Z. Wang, Control of low Reynolds number flows by means of fluid-structure interactions, Progress in Aerospace Sciences 64 (2014) 17–55. doi:10.1016/j.paerosci.2013.07.004.
URL http://www.sciencedirect.com/science/article/pii/S0376042113000857

[10] L. Ferguson, P. Seshaiyer, R. Gordnier, P. Attar, Computational modeling of coupled membrane-beam flexible wings for micro air vehicles, in: 48th AIAA/ASME/ASCE/AHS/ASC Structures, Structural Dynamics, and Materials Conference, American Institute of Aeronautics and Astronautics, 2007, dOI: 10.2514/6.2007-1787.
URL https://arc.aiaa.org/doi/abs/10.2514/6.2007-1787

[11] J. Babcock, R. Albertani, G. Abate, Experimental Estimation of the Rotary Damping Coefficients of a Pliant Wing, Journal of Aircraft 49 (2) (2012) 390–397. doi:10.2514/1.C031161.
URL https://doi.org/10.2514/1.C031161

[12] A. Song, K. Breuer, Dynamics of a Compliant Membrane as Related to Mammalian Flight, in: 45th AIAA Aerospace Sciences Meeting and Exhibit, American Institute of Aeronautics and Astronautics, 2007, dOI: 10.2514/6.2007-665.
URL https://arc.aiaa.org/doi/abs/10.2514/6.2007-665

[13] R. M. Waldman, K. S. Breuer, Shape, lift, and vibrations of highly compliant membrane wings, in: 43rd Fluid Dynamics Conference, American Institute of Aeronautics and Astronautics, 2013, dOI: 10.2514/6.2013-3177.
URL https://arc.aiaa.org/doi/abs/10.2514/6.2013-3177

[14] B. Stanford, P. Ifju, R. Albertani, W. Shyy, Fixed membrane wings for micro air vehicles: Experimental characterization, numerical modeling, and tailoring, Progress in Aerospace Sciences 44 (4) (2008) 258–294. doi:10.1016/j.paerosci.2008.03.001.
URL http://www.sciencedirect.com/science/article/pii/S0376042108000250

[15] O. M. Curet, A. Carrere, R. Waldman, K. S. Breuer, Aerodynamic Characterization of a Wing Membrane with Variable Compliance, AIAA Journal 52 (8) (2014) 1749–1756. doi:10.2514/1.J052688.
URL https://doi.org/10.2514/1.J052688

[16] W. McCroskey, L. Carr, K. McAlister, Dynamic stall experiments on oscillating airfoils, AIAA Journal 14 (1) (1976) 57–63. doi:10.2514/3.61332.
URL http://dx.doi.org/10.2514/3.61332

[17] W. McCroskey, The phenomenon of dynamic stall, in: Von Karman Inst. for Fluid Dynamics Unsteady Airloads and Aeroelastic Probl. in Separated and Transonic Flow, 1981.

[18] L. W. Carr, Progress in analysis and prediction of dynamic stall, Journal of Aircraft 25 (1) (1988) 6–17. doi:10.2514/3.45534.
URL http://dx.doi.org/10.2514/3.45534

[19] F. Coton, R. Galbraith, Experimental study of dynamic stall on a finite wing, Aeronautical Journal 103 (1023) (1999) 229 – 236.

[20] R. Cummings, S. Morton, S. Siegel, Numerical predictions and wind tunnel experiment for a pitching unmanned combat air vehicle, in: Aerospace Sciences Meetings, American Institute of Aeronautics and Astronautics, 2003, pp. –. doi:10.2514/6.2003-417.
URL http://dx.doi.org/10.2514/6.2003-417

[21] T. Beddoes, Onset of leading edge separation effects under dynamic conditions and low mach numbers, in: 34th Annual National Forum of the American Helicopter Society, American Helicopter Society, 1978.

[22] G. W. Reich, F. E. Eastep, A. Altman, R. Albertani, Transient Poststall Aerodynamic Modeling for Extreme Maneuvers in Micro Air Vehicles, Journal of Aircraft 48 (2) (2011) 403–411. doi:10.2514/1.C000278.
URL https://doi.org/10.2514/1.C000278

[23] N. Osterberg, Experimental Investigation of Dynamic Stall on Pliant Wings for Micro Air Vehicles, in: 54th AIAA Aerospace Sciences Meeting, American Institute of Aeronautics and Astronautics, 2016, dOI: 10.2514/6.2016-0146.
URL https://arc.aiaa.org/doi/abs/10.2514/6.2016-0146

[24] P. Masarati, M. Morandini, T. Solcia, A membrane element for micro-aerial vehicle fluid-structure interaction, in: P. Eberhard, P. Ziegler (Eds.), 2nd Joint International Conference on Multibody System Dynamics, Stuttgart, Germany, 2012.

[25] M. Alioli, M. Morandini, P. Masarati, Coupled multibody-fluid dynamics simulation of flapping wings, in: ASME IDETC/CIE, Portland, OR, 2013, DETC2013-12198. doi:10.1115/DETC2013-12198.

[26] M. Alioli, M. Morandini, P. Masarati, T. Carpenter, R. Albertani, Nonlinear membrane inverse finite element model for pliant wings, in: SCITECH, Kissimmee, FL, 2015, AIAA2015-2051. doi:10.2514/6.2015-2051.

[27] T. J. Carpenter, R. Albertani, Aerodynamic load estimation: Pressure distribution from virtual strain sensors for a pliant membrane wing, in: 54th AIAA/ASME/ASCE/AHS/ASC

Structures, Structural Dynamics, and Materials Conference, 2013, doi:10.2514/6.2013-1917.

[28] M. Goman, A. Khrabrov, State-space representation of aerodynamic characteristics of an aircraft at high angles of attack, Journal of Aircraft 31 (5) (1994) 1109–1115. doi:10.2514/3.46618.
URL http://dx.doi.org/10.2514/3.46618

[29] E. C. Polhamus, A concept of the vortex lift of sharp-edge delta wings based on a leading-edge-suction analogy (nasa tn d-3767), Tech. rep., Langely Research Center, NASA (1966).

[30] T. J. Carpenter, Predicting Aerodynamic Loads on Highly Flexible Membrane Wings, Ph.D. thesis, Oregon State University (jun 2015).
URL http://hdl.handle.net/1957/56376

[31] J. Anderson, Introduction to Flight, 7th Edition, McGraw-Hill Education, New York, NY, 2011.

[32] E. C. Polhamus, A concept of the vortex lift of sharp-edge delta wings based on a leading-edge-suction analogy, Tech. Rep. NASA-TN-D-3767, NASA (Dec. 1966).
URL https://ntrs.nasa.gov/search.jsp?R=19670003842

[33] R. Sheldahl, P. Klimas, Aerodynamic characteristics of seven symmetrical airfoil sections through 180-degree angle of attach for use in aerodynamic analysis of vertical axis wind turbines, Tech. rep., Sandia National Laboratories (1981).

[34] P. Masarati, M. Morandini, P. Mantegazza, An efficient formulation for general-purpose multibody/multiphysics analysis, J. of Computational and Nonlinear Dynamics 9 (4) (2014) 041001, doi:10.1115/1.4025628.

[35] A. Logg, K.-A. Mardal, G. Wells (Eds.), Automated Solution of Differential Equations by the Finite Element Method, Vol. 84 of Lecture Notes in Computational Science and Engineering, Springer Berlin Heidelberg, Berlin, Heidelberg, 2012.

[36] J. C. Simo, M. S. Rifai, A class of mixed assumed strain methods and the method of incompatible modes, Intl. J. Num. Meth. Engng. 29 (8) (1990) 1595–1638, doi:10.1002/nme.1620290802.

[37] U. Andelfinger, E. Ramm, EAS-elements for two-dimensional, three-dimensional, plate and shell structures and their equivalence to HR-elements, Intl. J. Num. Meth. Engng. 36 (8) (1993) 1311–1337, doi:10.1002/nme.1620360805.

[38] J. Hoffman, C. Johnson, Computational Turbulent Incompressible Flow, Vol. 4 of Applied Mathematics: Body and Soul, Springer, 2007, doi:10.1007/978-3-540-46533-1.

[39] V. John, Slip with friction and penetration with resistance boundary conditions for the Navier Stokes equations - numerical tests and aspects of the implementation, Journal of Computational and Applied Mathematics 147 (2) (2002) 287–300, doi:10.1016/S0377-0427(02)00437-5.

[40] J. Hoffman, J. Jansson, R. Vilela De Abreu, Adaptive modeling of turbulent flow with residual based turbulent kinetic energy dissipation, Special Issue on Modeling Error Estimation and Adaptive Modeling 200 (3740) (2011) 2758–2767. doi:10.1016/j.cma.2010.11.016.
URL http://www.sciencedirect.com/science/article/pii/S0045782510003403

[41] G. Quaranta, P. Masarati, P. Mantegazza, A conservative meshfree approach for fluid structure interface problems, in: M. Papadrakakis, E. Onate, B. Schrefler (Eds.), Int. Conf. on Computational Methods for Coupled Problems in Science and Engineering, Coupled Problems 2005, CIMNE, Barcelona, 2005, Santorini, Greece, 2005.

[42] R. M. Waldman, K. S. Breuer, Shape, lift, and vibrations of highly compliant membrane wings, in: 43rd Fluid Dyn. Conf., San Diego, CA, United states, 2013, pp. American Institute of Aeronautics and Astronautics (AIAA) –.

[43] A. Pelletier, T. J. Mueller, Low Reynolds number aerodynamics of low-aspect-ratio, thin/flat/cambered-plate wings, Journal of Aircraft 37 (5) (2000) 825–832. doi:10.2514/2.2676.
URL http://dx.doi.org/10.2514/2.2676

[44] W. Oswald, General formulas and charts for the calculation of airplane performance (NACA-TR-408), Tech. rep., U.S. Department of Commerce, National Technical Information Service (1933).

[45] E. Lillberg, R. Kamakoti, W. Shyy, Computation of unsteady interaction between viscous flows and flexible structure with finite inertia, in: 38th Aerospace Sciences Meeting and Exhibit, American Institute of Aeronautics and Astronautics, 1999, dOI: 10.2514/6.2000-142.
URL https://arc.aiaa.org/doi/abs/10.2514/6.2000-142

[46] R. E. Gordnier, P. J. Attar, Impact of flexibility on the aerodynamics of an aspect ratio two membrane wing, Journal of Fluids and Structures 45 (2014) 138–152. doi:10.1016/j.jfluidstructs.2013.10.004.
URL http://www.sciencedirect.com/science/article/pii/S0889974613002235

[47] N. Osterberg, Experimental Investigation of Dynamic Stall on Pliant Wings for Micro Air Vehicles, in: 54th AIAA Aerospace Sciences Meeting, American Institute of Aeronautics and Astronautics, 2016, dOI: 10.2514/6.2016-0146.
URL https://arc.aiaa.org/doi/abs/10.2514/6.2016-0146

[48] R. Albertani, B. Stanford, P. Ifju, Unsteady Mechanical Aspects of Flexible Wings: Experimental Investigation of Biologically Inspired MAVs, in: MAV07 3rd US-European Competition and Workshop on MAV Systems & European Micro Air Vehicle Conference and Flight Competition 2007, ISAE-SUPAERO, Toulouse, France, 2007.
URL http://aeromav.free.fr/MAV07/session/plenary/SESSION%203/MAV07-PLEN%203-3%20Albertani/Albertani.pdf

[49] U. K. Chakravarty, R. Albertani, Experimental and Finite Element Modal Analysis of a Pliant Elastic Membrane for Micro Air Vehicles Applications, Journal of Applied Mechanics 79 (2) (2012) 021004–021004–6. doi:10.1115/1.4005569.
URL http://dx.doi.org/10.1115/1.4005569

[50] R. M. Waldman, K. S. Breuer, Shape, lift, and vibrations of highly compliant membrane wings, in: 43rd Fluid Dynamics Conference, American Institute of Aeronautics and Astronautics, dOI: 10.2514/6.2013-3177.
URL https://arc.aiaa.org/doi/abs/10.2514/6.2013-3177

[51] V. Buljak, Inverse analyses with model reduction: proper orthogonal decomposition in structural mechanics, Springer Science & Business Media, 2011.

Modeling effects of membrane tension on dynamic stall for thin membrane wings

Mattia Alioli[1], Pierangelo Masarati[2], Marco Morandini[3,*]

Politecnico di Milano, Dipartimento di Scienze e Tecnologie Aerospaziali, via La Masa 34, 20156, Milano, Italy

Roberto Albertani[4,*], Trenton Carpenter[5,*]

Oregon State University, Mechanical Engineering, 204 Rogers Hall Corvallis, 97330 OR

Abstract

An approach for predicting time varying aerodynamic loads on a pitching membrane wing due to rotational pitching and steady airflow is presented. The proposed model utilizes potential flow theory for a thin cambered airfoil with finite span, combined with a linearized representation of the membrane physics to predict lift under static conditions. ~~Quasi-steady~~ Quasi-steady rotational effects and added mass effects are considered in a classic potential flow approach, modified for a membrane airfoil. A ~~high fidelity~~ high-fidelity numerical model has been developed as well, coupling a viscous fluid solver and a ~~non linear~~ non-linear membrane structural model, to predict the configuration of the system under static and unsteady loads. Moving Least Squares are used to map the structural and fluid interface kinematics and loads during the ~~fluid structure co simulation. Comparisons of the~~ fluid-structure co-simulation. The static and dynamic lift predictions of the two models are ~~made~~ compared to wind tunnel data, and show reasonable accuracy over a wide range of flow conditions~~($Re = 50k - 84k$)~~, reduced frequency~~($k = 0, 0.05$, 0.1), and membrane pre-tensions ($\lambda_o = 1.02, 1.058, 1.085$~~ and ~~$\infty$).~~ membrane pretension.

Keywords: dynamic stall; ~~fluid structure~~ fluid-structure interaction; MAV; membrane wings;

Nomenclature

α	Angle of attack (°)
α_o	Zero lift angle of attack (°)
Æ	Wing aspect ratio
c	Normalized chord length
ϵ	Strain of the membrane
ε	~~Ozwald~~ Oswald efficiency
K_p	Potential flow lift constant
K_i	Induced drag constant
P	Pressure (N)
E	Modulus of elasticity (Pa)
ν	Membrane Poisson ratio
h	Membrane thickness (m)
λ	~~$= 1 + \epsilon$,~~ Membrane stretch ratio due to deformation
λ_o	Membrane stretch ratio due to pretension
ρ	Membrane material density (kg/m^3)
Re	Reynolds Number
U_∞	Free stream flow velocity (m/s)
k	Reduced frequency
X_{st}	Degree of trailing edge separation, static
$X(t)$	Degree of trailing edge separation, dynamic
~~$C_{L,dat}$~~ $C_{L,st,dat}$	Coefficient of lift, static, wind tunnel data
$C_{L,d,dat}$	Coefficient of lift, dynamic, wind tunnel data
$C_{L,p}$	Coefficient of lift, static attached potential flow
$C_{L,v}$	Coefficient of lift, due to leading edge separation
$C_{L,mem}$	Coefficient of lift, due to membrane displacement
$C_{L,att}$	Coefficient of lift, total static attached flow
$C_{L,sep}$	Coefficient of lift, static separated flow
$C_{L,st}$	Coefficient of lift, static conditions
$C_{L,qs}$	Coefficient of lift, quasi-steady dynamic condition
$C_{L,d}$	Coefficient of lift, dynamic conditions
$C_{L,fsi}$	Coefficient of lift, ~~fluid structure~~ fluid-structure s

1. Introduction

Artificial micro flyers such as micro air vehicles (MAV) require highly agile maneuverability while maintaining benign flying characteristics in the entire flight envelope to prevent expanding the pilot or the autonomous flight control system beyond its capability. A significant body of early work on

*Corresponding author

Email addresses: mattia.alioli@polimi.it (Mattia Alioli), pierangelo.masarati@polimi.it (Pierangelo Masarati), marco.morandini@polimi.it (Marco Morandini), roberto.albertani@oregonstate.edu (Roberto Albertani), trenton.carpenter@gmail.com (Trenton Carpenter)

[1]Ph.D. & Research Assistant, Dipartimento di Scienze e Tecnologie Aerospaziali

[2]Professor, Dipartimento di Scienze e Tecnologie Aerospaziali

[3]Associate Professor, Dipartimento di Scienze e Tecnologie Aerospaziali

[4]Associate Professor, Mechanical Engineering

[5]Ph.D., Mechanical Engineering

theoretical predictive models and experimental validation, including the fluid- structure interactions characterization, have elucidated the superior aerodynamic characteristics of flexible-wing MAVs, demonstrating the benign effects of a flexible wing with respect to a rigid configuration [1, 2, 3, 4] in steady flight conditions. A massive amount of work on flexible wings in unsteady conditions was performed by several authors on flapping wings in insects, birds and artificial wings in the last twenty years. A general view of aeroelastic implications on the aerodynamics of flapping wings was presented [5], as well as specific studies on effects of membrane wings on animal flight [6, 7] with specific applications on bats. Aeroelastic features on fixed wing configurations of flexible and membrane-wings in unsteady conditions have been presented including experimental studies [8, 9] and theoretical models [10]. Further research on fixed-wings MAV with membrane flexible wings was recently performed in unsteady conditions correlating membrane pretension levels, dynamic variation of wing pitching and angle of attack with the rotary-damping coefficients [11]. Specific research on wing membrane dynamics was also performed including vibrations [12, 13] and membrane pressrun a tailoring effects of wing performance [14, 15].

Dynamic stall of pitching airfoils is a includes a series of complex phenomena due to the delayed transient response of the fluid flow around the airfoil, cfr.[16, 17, 18, 19, 20, 21]. [16, 22, 17, 18, 23, 24]. Rigid wings were experimentally investigated in wind tunnel tests used for validation of semi-empirical numerical models for transient post-stall aerodynamics for perching-flight mechanics studies [25]. Membrane-wings aerodynamics during dynamic stall conditions experimental results were performed presenting results on the correlation between membrane pretension, wing-pitch kinematics, Reynolds number and membrane shape at various reduced frequencies values [26]. In this work, a predictive lift model is presented for the dynamic stall phenomena of a dynamically pitching, perimeter reinforced, membrane wing. A combined analytic and empirical model is presented which utilizes existing and novel formulations of the dynamic aero-elastic aeroelastic phenomena surrounding the problem.

A membrane finite element formulation, implemented in a multibody formulation, cfr. [27], is used in co-simulation co-simulation with a fluid dynamics solver to predict the configuration of the system under static and unsteady loads, as shown in [28, 29]in [30, 29].

The experimental setup used in this work allows to can accurately measure the full field three dimensional full-field three-dimensional displacement and strain over a memebrane membrane wing in wind tunnel testing conditions. Digital Image Correlation (DIC) is used to measure strains and, in conjunction with a load cell, is used to measure stresses , strains, and to estimate stresses and measure aerodynamic forces exerted on the membrane wing during wind tunnel testing. DIC measurements were used to generate virtual strain sensors on the surface of the membrane [31].

Analytical and numerical results, along with experimental measurements of actual membrane wing artifacts subjected to a variety of steady and unsteady flow conditions, are used to validate the proposed formulation.

2. Analityeal Analytical Methods

The dynamic stall model presented in this work accounts for variation of lift due to a combination of leading edge separation, membrane deformation, quasi-steady and and quasi-steady and transient delayed lifting effects from dynamic pitching. This model utilizes a state-space state-space representation of the time varying, delayed stall effects due to dynamic motion [20]. For static angles of attack (AOA), loads generated by leading edge separation are modeled using a leading edge suction analogy for thin airfoils [32]. The position of Moreover, the position of the trailing edge separation , for static AOA, is estimated using wind tunnel test data to tune an empirical trailing edge separation model. The static contribution of lift from membrane deformation is modeled by applying several assumptions to the physics of the membrane. This method is detailed in Carpenter [33], ; in the following section, a summary of this approach is discussed.

2.1. Static Lift Model

The static lifting curve, which is used as the "backbone" of the dynamic stall prediction, is generated by first defining two different lift curves (under static AOA conditions); the first for fully attached flow, and the second for fully separated flow. Transition between these two states due to stall , is determined using wind tunnel test data.

In this approach, the main contributions of lift on to lift of a thin membrane wing, for static AOA, are assumed to be from potential flow, leading edge separation, and cambering due to membrane displacement. The total lift under attached flow conditions[6] can thus be expressed, cfr. [33], as

$$C_{L,att} = C_{L,p} + C_{L,v} + C_{L,mem}. \tag{1}$$

In Eq. (1), $C_{L,p}$ is the lift coefficient for a finite length wing due to potential flow, i.e., $C_{L,p} = K_p(\alpha + \alpha_o)$, where α is the angle of attack (AOA), α_o is the AOA at zero lift ($C_{L,p} = 0$), and $K_p = \frac{2\pi}{\left(1+\frac{2\pi}{\pi \varepsilon \mathcal{R}}\right)}$ is the potential flow constantas defined in Carpenter [33], see e.g. [34][7]. Assuming that the flow reattaches past the leading edge separation bubble, the component of contribution to lift due to

[6] With The term "attached" flow we mean refers here to a flow which reattaches beyond the leading edge separation bubble and remains attached until the trailing edge.

[7] The contribution of lift due to unstable membrane displacement at zero AOA is accounted for in $C_{L,p}$, as shown in [33]. This model assumes the direction of unstable displacement to be in the direction of positive lift, thus generating a positive lift contribution, and does not consider the bifurcating effect which would occur if the wing was to sweep from a positive AOA to a large negative AOA.

leading edge separation, $C_{L,v}$, for a rectangular wing can be written as $C_{L,v} = (K_p - K_p^2 K_i)\cos(\alpha)\sin^2(\alpha)$, where $K_i = \frac{1}{\pi\varepsilon AR}$ is the induced drag constant ~~[33]~~[35]. Finally, $C_{L,mem}$ is the value of lift due to membrane displacement. To come to an expression for $C_{L,mem}$, it was assumed that the membrane displacement can be modeled as a circular arc, and the load applied to the membrane was an evenly distributed pressure. ~~In this way, the~~ The membrane is modeled as massless, linear elastic, constrained along all edges, with constant internal tension due to deformation and constant positive ~~pre-tension~~ pretension in its reference configuration. Provided these assumptions, the state of membrane deformation can be equated to an aeroelastic coefficient, $Ae = \frac{Eh}{\frac{1}{2}\rho U_\infty^2 c} = \frac{Eh}{qc}$, where E is the linear modulus of elasticity of the membrane, h is the membrane thickness, ρ is the density of the fluid, U_∞ is the free stream velocity of the fluid, c is the wing chord, and q is the dynamic pressure. If the membrane out-of-plane displacement is assumed to fit the form of a circular arc, and the value of maximum displacement normalized to the chord length is defined as z, then it can be shown that: $\frac{C_L}{Ae} = f(\lambda_o, z)$, where f is a function to be determined and λ_o is defined as the stretch ratio due to pretension, i.e., $\lambda = (1+\epsilon)$, where ϵ is the strain of the membrane due to deformation and/or pretension.

Using the potential flow solutions for a circular arc airfoil, a relationship between the AOA and membrane displacement (normalized to the chord), $z = z_{max}/c$, can be found for a finite aspect ratio rubber membrane wing~~,~~:

$$\alpha + \sin^{-1}\left(2\eta\frac{Ae}{K_p}(\kappa - \lambda_o\phi)\right) - \frac{\phi}{4} = 0 \tag{2}$$

where ϕ and κ are the arc segment angle and radius of curvature respectively, as shown in ~~Carpenter [33].~~ Fig. 1, and $\eta = (1 + \frac{1}{AR})$. For a chord length, c, equal to unity, ϕ and κ can be defined in terms of normalized max out-of-plane displacement, $z = z_{max}/c$, as:

$$\phi = 2\sin^{-1}\left(\frac{\kappa}{2}\right) \tag{3}$$

$$\kappa = \frac{8z}{4z^2+1}. \tag{4}$$

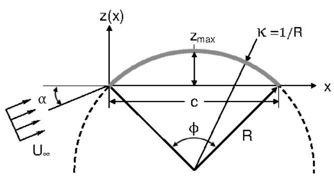

Figure 1: Geometry of a circular arc segment used to generalize the chordal shape of a displaced membrane airfoil.

Thus, given α, material properties and flow conditions, Eq. (2) can be used to find the value of camber z. Substituting z into Eq. (4), κ into Eq. (3), the value of lift due to membrane displacement for a finite aspect ratio wing can be defined as:

$$C_{L,mem} = K_p\left(\sin\left(\alpha + \frac{\phi}{4}\right) - \sin(\alpha)\right). \tag{5}$$

To model the lift coefficient of a separated flow, ~~we consider test data~~ test data are considered for angles of ~~attach~~ attack beyond complete stall. Extending an empirical two dimensional lift model for separated flow (obtained considering wind tunnel test data [36]) to a finite aspect ratio wing, the lift coefficient for three dimensional separated flow can be approximated as

$$C_{L,sep} = \frac{\pi\sin(2\alpha)}{3 + \frac{1}{\varepsilon AR}}. \tag{6}$$

Considering the attached flow model from Eq. (1) and the separated flow model from Eq. (6), a complete static lift model which transitions from fully attached to fully separated flow conditions can be defined. Let the degree of trailing edge separation be defined as $0 \le X_{st} \le 1$, where a value of $X_{st} = 1$ represents a condition of fully attached flow, and a value of $X_{st} = 0$ represents fully separated flow. Thus:

$$C_{L,st} = C_{L,att}X_{st} + C_{L,sep}(1 - X_{st}), \tag{7}$$

with

$$X_{st} = \frac{1}{\left[1 + \left[\left(\frac{\alpha}{\alpha^*}\right)^2\right]^{n_1}\right]^{n_2}} \tag{8}$$

The degree of separation model X_{st} used in this study is thus a blending function, so that the transition between the two models is smooth. ~~The~~ For a given wing configuration and flow condition, the factors α^*, n_1, and n_2 are computed ~~, for a given wing configuration and flow condition,~~ using wind tunnel test data. A least squares regression is used to minimize the error between lift data and the static AOA model, $C_{L,st}$.

2.2. Dynamic Stall Model

The dynamic stall model used in this work is a time varying, physics based model [20]. ~~Quasi-steady~~ Quasi-steady rotational effects (i.e., circulation changes and boundary convection lag), which equate to instantaneous delayed lift and added mass loads, are considered using a potential flow approach for a thin airfoil. Considering a thin airfoil pitching about a quarter chord axis, and applying the thin airfoil theory, an effective AOA can be defined to account for ~~quasi-steady~~ quasi-steady rotational flow effects, viz., $\alpha_{qs} = \alpha + \frac{c}{2U_\infty}\dot{\alpha}$. Substituting this effective AOA into $C_{L,st}$ from Eq. (8), a model which describes ~~quasi-steady~~

quasi-steady dynamic lift is obtained as follows,

$$C_{L,qs} = C_{L,att}(\alpha_{qs})X_{st}(\alpha_{qs}) + C_{L,sep}(\alpha_{qs})(1 - X_{st}(\alpha_{qs})) \tag{9}$$

A first order differential equation, which describes the transient/relaxation behavior of the separation point, is used to account for the delay (with respect to time) of the separation point in its progression along the airfoil, as AOA increases into stall regime, viz.

$$\tau_1 \dot{X}_d + X_d = X_{st}(\alpha - \tau_2\dot{\alpha}) \tag{10}$$

where τ_1 is a dynamic separation point relaxation time constant. Coefficient τ_2 is a ~~quasi–steady~~ quasi-steady separation point time scaling constant, $\tau_2 = \tau_2^* \frac{c}{2U_\infty}$, where τ_2^* is a tuning parameter. Assuming a known kinematic pitching motion of the airfoil about the quarter chord position, where $\hat{\alpha}_s$ and $\dot{\hat{\alpha}}_s$ are the known initial static AOA and pitch rate, Eq. 10 can be solved for $X_d(t)$ using a numeric ordinary differential equation solver and an initial condition of $X_d(t)|_{t=0} = X_{st}(\hat{\alpha}_s - \tau_2\dot{\hat{\alpha}}_s)$. $X_d(t)$ represents the dynamic separation point of the cambered airfoil due to a time varying pitching motion. With ~~quasi–steady~~ quasi-steady separation effects and transient separation effects modeled, a complete dynamic stall model is defined for a given pitching motion as,

$$C_{L,d} = C_{L,att}(\alpha_{qs})X_d(t) + C_{L,sep}(\alpha_{qs})(1 - X_d(t)) \tag{11}$$

3. Coupled ~~Fluid–Structure~~ Fluid-Structure Simulation

The overall approach adopted here was to use two different codes, i.e., a flow solver and a structural solver, and to exchange configuration and loads data between the two. This was achieved by adopting a tightly coupled ~~fluid–structure co–simulation~~fluid-structure co-simulation, in which the structural problem is solved using the free ~~general–purpose~~ general-purpose multibody dynamics solver MBDyn[8], developed at Politecnico di Milano [37], and the fluid problem is solved using a dedicated solver based on FEniCS[9] [38, pp. 171-222]. ~~FEniCS allows to define~~ With few high-level Python statements, FEniCS supports the definition of the discretized weak form of complex systems of Partial Differential Equations (~~PDE~~PDEs), and ~~corresponding discretization and iteration strategies, in terms of a few high–level Python statements which inherit the mathematical structure of the problem, and from which low–level code is automatically generated [28, 29]~~can drive the solution of the ensuing nonlinear problem. The FEniCS Form Compiler (FFC) automatically generates the low-level C++ code that efficiently computes the residual vector and its Jacobian matrix for the problem at hand. A tight coupling, i.e. the exchange between the viscous flow and the structural solver of configuration and loads data at each iteration until mutual convergence was found necessary, due to the strong interaction of the fluid and the membrane structure in this problem. The computational analyses are assessed with experimental results. Specifically, we highlight our ongoing efforts geared towards developing an integrated computational and experimental approach to perform aeroelastic analyses of membrane wings within various configurations.

[8] http://www.mbdyn.org/.

[9] http://fenicsproject.org/.

Structural Solver. ~~The membrane element~~A four-node isoparametri membrane element, based on second Piola-Kirchhoff type membranal resultants, is implemented in MBDyn for the analyses in this work~~is a four–node isoparametric element, based on second Piola–Kirchhoff type membranal resultants~~ [27]. The membranal stresses are computed as functions of their ~~work–conjugated Green–Lagrange~~ work-conjugated Green-Lagrang strains. The classical Enhanced Assumed Strains (EAS) method [39] is exploited to improve the response of the element~~:~~; seven additional variables for each membrane element are added to the strain vector [40].

Fluid Solver. The fluid dynamics code is based on a stabilized finite element approximation of the unsteady ~~Navier–Stokes~~ Navier-Stokes equations, often referred to in the literature as General Galerkin, or G2, method [41]. The ~~so–called~~ so-called ALE cG(1)cG(1) formulation, with friction boundary conditions ~~[41, 42]~~[41, 43], was chosen. ~~For~~ In short, G2 is a weighted ~~least–squares~~ least-squares stabilized Galerkin finite element method in ~~space–time~~space-time. The stabilization of G2 acts as an automatic turbulence model in the form of a generalized artificial viscosity model acting selectively on the smallest scales of the mesh [44]. In particular, the stabilized cG(1)cG(1) method is a type of G2 method with continuous piecewise linear *trial* functions both in time and space, for both velocity and pressure, and continuous piecewise linear *test* functions in space and piecewise constant *test* functions in time.

Aeroelastic Coupling. The coupling of viscous flow and structural solvers used in this work requires the definition of a common interface. In particular, the multibody solver is coupled with the external fluid dynamics code by means of a ~~general–purpose~~general-purpose, meshless boundary interfacing approach based on Moving Least Squares with Radial Basis Function [45]. ~~The mapping produces~~ This is accomplished by precomputing a linear interpolation operator, $\mathcal{H}$, that ~~allows to compute~~ computes the interface aerodynamic nodes displacement $\mathbf{x}_a$ from the structural nodes displacements~~$\mathbf{x}_s$, namely~~: $\mathbf{x}_a = \mathcal{H}\mathbf{x}_s$. To guarantee the conservation of the (virtual) work done in the two domains, the linear operator that computes the aerodynamic forces applied to the structural nodes, $\mathbf{f}_s^a$, is the transpose of the interpolation matrix $\mathcal{H}$, viz.: $\mathbf{f}_s^a = \mathcal{H}^\top \mathbf{f}_a^a$. The computer implementation of the ALE technique requires the formulation of a ~~mesh–update~~ mesh-update procedure that assigns ~~mesh–node~~ mesh-node velocities and displacements at each time step. The mesh deformation process moves the fluid mesh nodes according to a linear elastic "~~fictitiuos" problem [28]~~fictitious" problem, where the elastic modulus of each element is proportional to the inverse of its volume. If the volume of an element becomes negative as a consequence of the displacement of the interface nodes, the elastic modulus of such an element is increased and the linear elastic problem is solved again.

4. Modeling

Aerodynamic tests were performed in a low speed wind tunnel. Lift and membrane displacement for a wing pitching with static and dynamic AOA were measured. Measured data were compared with ~~the predicitons~~ predictions from the two previously discussed methods. Tests were conducted on wing models with varying membrane pretension, subject to various flow conditions and pitching rates. The test matrix was built by varying the membrane pretension (λ_o), the flow velocity (U_∞), the pitch rate ($\dot{\alpha}$), the reduced frequency (k), and the starting pitch angle (α_{st}). The pitching amplitude (α_{amp}) was held constant at 10° ~~peak to peak~~peak-to-peak, and the pitching axis was held constant at 25% chord position throughout the tests.

4.1. Wind Tunnel Testing

The test article used in the wind tunnel is a 2:1 aspect ratio, rectangular, perimeter reinforced membrane wing. The wing, which has a span of 280 mm and chord of 140 mm, is made with two shaped steel frames ($E = 210$ GPa, $\nu = 0.3$, $\rho = 7800$ kg/m^3, with a frame width and thickness of 5 mm and 1 mm, respectively). A rubber latex membrane ($E = 1.14$ MPa, $\nu = 0.4$ and $\rho = 960$ kg/m^3), held at a prescribed ~~in plane pre-tension~~in-plane pretension, was sandwiched between the two steel frames. Images of the actual test article can be seen in Fig. 2, and a schematic of the test ~~set up~~ set-up is illustrated in Fig. 3.

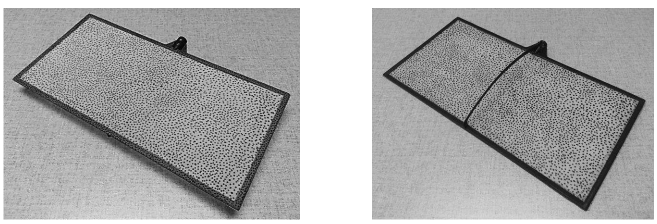

(a) Top View (b) Bottom View

Figure 2: 2:1 membrane wing, with steel perimeter and speckled rubber latex membrane.

A range of flow conditions with Reynolds number between 50k–100k were tested. Reduced frequency values of $k = \{0, 0.05, 0.1\}$ were used while operating ~~withing~~ within the pitching motor's operational envelope. Three target cambers were selected using Waldman's membrane displacement approach [46], resulting in three membrane

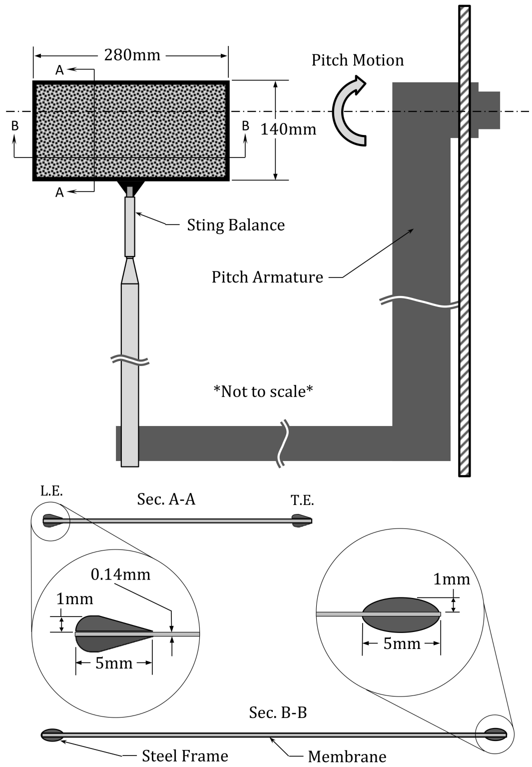

Figure 3: Wind tunnel pitching fixture and membrane wing with frame geometry.

wings with corresponding stretch ratio of $\lambda = \{1.02, 1.058, 1.085\}$. In addition to these stretch ratios, a relatively high value of λ was also tested in order to see the influence of the frame on the aerodynamics of the wing, compared to the frame plus a compliant airfoil. The test matrix is summarized in Fig. 4~~, where $Ae = \frac{Eh}{\frac{1}{2}\rho U_\infty^2 c} = \frac{Eh}{qc}$~~. In ~~Fig. 4~~that

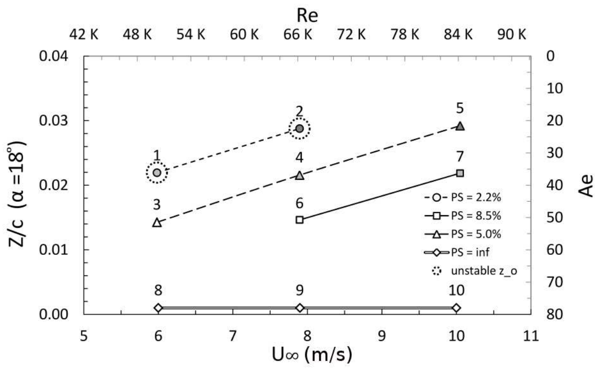

Figure 4: Predictions of membrane camber for different test conditions.

figure, each line represents a membrane wing model with different ~~pre-tension~~pretension (PS), each point represents a test condition (with a label corresponding to each unique test condition), and the points circled with a dotted line ~~representing~~ represent conditions of unstable membrane displacement at zero AOA. In addition to testing the four membrane configurations ($\lambda = \{1.02, 1.058, 1.085\}$ and $\lambda \rightarrow \infty$), a 2:1 flat plate was also tested to serve as a basis of comparison to a well known aerodynamic profile. The geometry of this 2:1 flat plate wing conformed to the leading edge, trailing edge and thickness dimensions defined by Mueller ~~[47]~~[48]. This flat plate ("Mueller" from now on) was tested for static AOA conditions and all dynamic AOA conditions. For each condition in Fig. 4, data ~~was~~ were collected at static AOA, for $\alpha = -2°$ to $30°$, at $2°$ increments. For all wing configurations, dynamic sweeps were performed using $\alpha_{st} = \{0°, 5°, 10°\}$, $\alpha_{amp} = 10°$, and $k = \{0.05, 0.1\}$. Finally, a commonly accepted ~~Ozwald~~ Oswald efficiency factor for rectangular wings of $\varepsilon = 0.9$ ~~[49]~~ [50] for all wings within the study is applied.

The ~~low speed~~ low-speed closed loop wind tunnel is capable of speeds from 1 to 18 m/s and has a 1.3 ~~x~~ × 1.5 m test section. Aerodynamic loads from the wing were measured by a six ~~degree of freedom~~ degree-of-freedom sting balance fixed directly at the trailing edge. The system was capable of simultaneously pitching, measuring aerodynamic loads and performing ~~non intrusive~~ non-intrusive displacement measurements via DIC. Load and angle channels were recorded at 500 Hz, and DIC images were taken at 500 frames per second[10]. Time varying data from the load cell were averaged to identify a measurement of the steady state coefficient of lift and drag for each test condition.

4.2. Numerical Modeling

The structural grid, implemented within the multibody simulation environment provided by MBDyn, consists of 8×16 ~~four node~~ four-node membrane elements, involving 153 structural nodes. To model the steel frame surrounding the membrane wing, 24 ~~three nodes beams~~ three-node beam elements were added to the structural model. The mass lumped in each node is computed from the latex rubber sheet portion associated with the node, which is uniformly distributed, and in addition, for the boundary nodes, from the portion of the steel frame associated with the node [29].

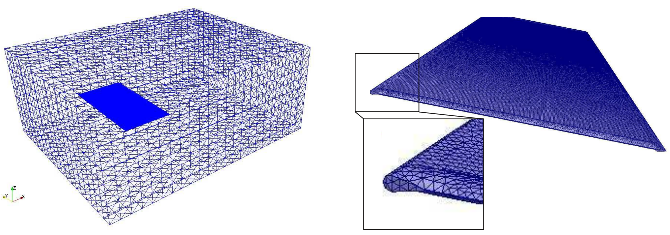

(a) CFD simulation domain. (b) Meshed membrane wing.

Figure 5: CFD domain.

[10]DIC measurements were averaged over the 500 snapshots which were taken at 500 Hz for a duration of 1 second.

The fluid simulation volume, shown in Fig. 5, consists of approximately 270k nodes and 1.4 ~~millions~~ million tetrahedrons with a cell width of 0.2 mm in the near wake region, and cells growing up to 10 mm near the simulation boundaries. At the domain inlet the velocity magnitude and direction are set as boundary conditions, while at the outlet a constant pressure is specified. The other four boundary walls are ~~characterised~~ characterized by a slip wall boundary condition. A "skin friction model" was used to simulate slip with (linear) friction and penetration with resistance boundary conditions on the wing surface ~~[28, 41, 42].~~ [41, 43]. This choice does not allow to completely resolve the boundary layer; it brings, however, substantial computational savings without completely compromisin the simulation accuracy. The leading and ~~the~~ trailing edge are ~~modelled~~ modeled as flexible, aerodynamically shaped supports, as shown in Fig. 5(b).

5. Results

To evaluate the ~~validity~~ ability of the proposed ~~approach~~ approaches of estimating dynamic lift due to pitching, experimental wind tunnel loads and membrane displacements are compared to the proposed ~~model~~ models under varying conditions of flow velocity, pretension, pitching frequency, and AOA pitching ranges. In Section 5.1, the ~~components composing~~ contributions to the static lift curve resulting from the analytical model (i.e., $C_{L,p}$, $C_{L,v}$, $C_{L,mem}$, $C_{L,att}$, $C_{L,sep}$, and X_{st}), are compared with time averaged, static test data, $C_{L,st,dat}$, and with the results from the coupled ~~fluid structure~~ fluid-structure analysis, $C_{L,fsi}$. In Section 5.2, dynamic (analytical) lift predictions, $C_{L,qs}$, and $C_{L,d}$, are compared with dynamic test data as ~~a function~~ functions of α and time for varying dynamic pitching conditions.

5.1. ~~Non Pitching~~ Non-Pitching Case

Fig. 6(a) shows the coefficient of lift with respect to AOA for the 2:1 "Mueller" flat plate, with a thickness of 3.2 mm. Thus, for this wing, the leading edge separation is minimal, i.e., $C_{L,v}(\alpha) = 0$. Since the wing is stiff, we assume $C_{L,mem} \approx 0$. Thus, $C_{L,p} = C_{L,att}$, meaning the calculation of potential flow should adequately model the flat plate for ~~pre stall~~ pre-stall AOA. Observing Fig. 6(a), it ~~can be~~ is noticed that for $\alpha < 12°$, the potential flow component of lift accurately predicts measured lift. For high AOA, wind tunnel data approaches $C_{L,sep}$ asymptotically as expected. Using data, $C_{L,att}$, and $C_{L,sep}$, a regression fit is used to generate X_{st}, from which $C_{L,st}$ can be calculated.

The error bars in Fig. 6(a) represent 95% confidence intervals; in most cases they are smaller in magnitude than the square points representing the measurement in the figure. To reduce figure complexity, confidence intervals will not be presented on further graphs.

Fig. 6(b) shows the results obtained with the perimeter reinforced membrane wing, where the membrane is

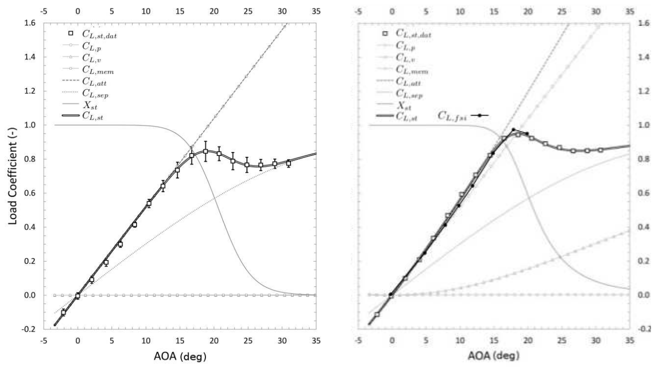

(a) 2:1 "Mueller" flat plate.

(b) Wing with "rigid" membrane.

Figure 6: Static lift model and wind tunnel data. (a) 2:1 "Mueller" flat plate, (b) membrane wing with "rigid" membrane.

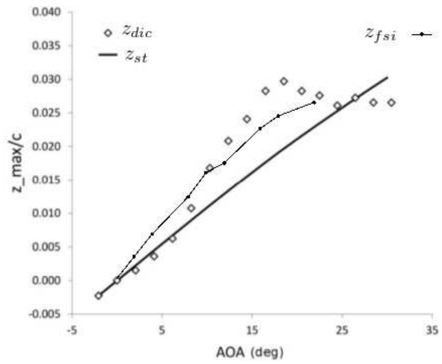

Figure 7: DIC and predicted displacement.

replaced with a thin "rigid" plate of comparable thickness. For this wing, leading edge separation is expected so that $C_{L,v}(\alpha) \neq 0$, while $C_{L,mem}$ is still driven to zero, thus $C_{L,att} > C_{L,p}$. As previously noted, $C_{L,att}$ accurately models lift for low angles of attack, and the data appears to converge toward $C_{L,sep}$ for large AOA, although slower than in the previous case. The lift coefficient predicted by the coupled ~~fluid–structure~~ fluid-structure analysis, $C_{L,fsi}$, is also shown in Fig. 6(b). It should be noted that for these rigid wings, $C_{L,st}$ are invariant to changes in flow velocity within the ranges of this study (Re = 50k–84k).

The analytical and numerical ~~model~~ models show good agreement with the experiments, for lift over the rigid wing prior to stall. In general, results from Fig. 6 ~~confirms~~ confirm that both models have the capability to accurately predict lift over a large range of static AOA, for the 2:1 rigid flat plate and for the 2:1 membrane wing with a rigid membrane, experiencing leading edge separation. Compliant membranes are considered next.

The predicted max camber, $z(\alpha)$, is compared with DIC measurements. Fig. 7 represents the (average) maximum measured and predicted static camber, z_{dic} and z_{st} respectively, for a flow velocity of $U_\infty = 8$ m/s (Re = 66k), and prestretch $\lambda_o = 1.058$ (or 5.8% average prestrain). The max camber, computed by the coupled ~~fluid–structure~~ fluid-structure simulation, z_{fsi}, is also reported for comparison.

The analytical predicted maximum camber fairly accurately models measured displacements up to about $\alpha = 8°$. Given the linearizing assumptions built into the prediction model for membrane displacements and loads, the resulting analytical model represents the physics of the system for small AOA. The abrupt change in the experimental displacement at $\alpha = 8°$ indicates that there is an interaction mode that is not captured in the analytical model. Given the analytical results of the membrane camber predictions presented above, it is expected that the estimated coefficient of lift will be slightly ~~under predicted~~ underpredicted for intermediate AOA, $\alpha = 8°$ to $18°$. The numerical predicted max camber z_{fsi}, instead, better reproduces measured displacements from $\alpha = 10$ deg. For α below this value, the numerical prediction is slightly ~~over–estimated~~over-estimated. Correlation between both models and experiments is nevertheless deemed acceptable, with the numerical model slightly ~~over–predicting~~ over-predicting the local membrane inflation for small AoAs.

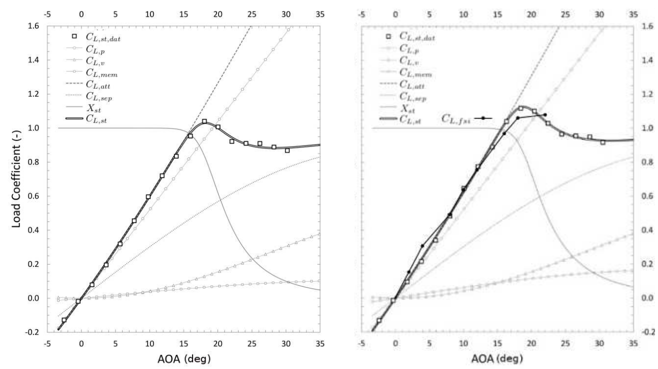

(a) 5.8% prestrain, Re = 50k.

(b) 5.8% prestrain, Re = 66k.

Figure 8: Static lift model, perimeter reinforced membrane wing.

Fig. 8(a) shows lift coefficient ~~verus~~ versus AOA for test condition "3" in Fig. 4, $\lambda_o = 1.058$, $U_\infty = 6$ m/s (Re = 50k), while Fig. 8(b) depicts test condition "4" in Fig. 4, $\lambda_o = 1.058$, $U_\infty = 8$ m/s (Re = 66k). Attached lift slope and peak lift are greater for the higher velocity case. This is due to the increased contribution of $C_{L,mem}$ and to the difference in dynamic pressure, as illustrated in Fig. 8. Both test conditions show a stable membrane at zero AOA, i.e., zero camber and thus zero lift at zero AOA, both for the experiment and the numerical ~~simualtions~~simulations. The static lift curve $C_{L,fsi}$ as given by the coupled ~~fluid–structure~~ fluid-structure analysis is also shown in Fig. 8(b) for comparison.

5.1.1. Effect on Flexible Wing

The lift and drag coefficients were computed, both for the experimental wind tunnel test and the ~~fluid–structure~~

fluid-structure simulation, by averaging their values over time. However, in some conditions the actual response is not stationary. Fig. 9 reports the time evolution of

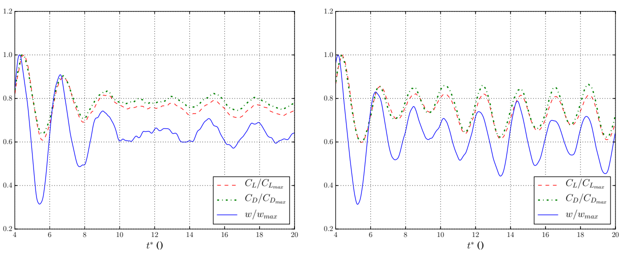

(a) $\alpha = 8$ deg. (b) $\alpha = 12$ deg.

Figure 9: Flexible membrane at 5.8% prestrain, $Re = 66$k. Mid-membrane point displacement and global C_L–C_D histories.

the numerical (~~high fidelity~~high-fidelity) aeroelastic system for two different values of AoA, $\alpha = 8$ and 12 deg, respectively, starting at non-dimensional time ~~$t^* = t\frac{V}{c} = 5$~~ $t^* = t\frac{V}{c} = 4$ to $t^* = 20$. Similar non stationary behavior of the wing membrane out of plane displacement and modal characteristics have been observed and reported in previous theoretical [51, 52] and experimental [53, 54, 55, 56, 9] research work. The evolution of the ~~normalised~~ normalized aerodynamic coefficients C_L and C_D, and the membrane maximum amplitude, w, is shown. The values are ~~normalised~~ normalized with respect to their maximum value.

As depicted in Fig. 9, the maximum value of deformation came after about ~~$t^* = t\frac{V}{c} \approx 5$~~$t^* \approx 5$, and reaches a "steady" value after about $t^* = 20$ chords for the membrane at $\alpha = 8$ deg, while for $\alpha = 12$ deg the oscillation continue beyond $t^* = 20$.

~~To analyze the effects of aeroelastic deformation on the flow structure,~~ Fig. 10 shows the deformation contour at different times ~~$t^* = t\frac{V}{c}$~~t^*, for the membrane at 5.8% prestrain, ~~$V = 8$~~$U_\infty = 8$ m/s and $\alpha = 8$ deg.

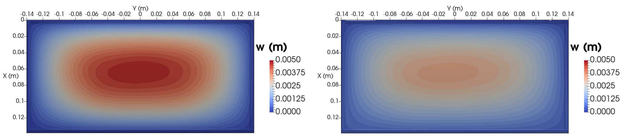

(a) $t^* = 4$. (b) $t^* = 10$.

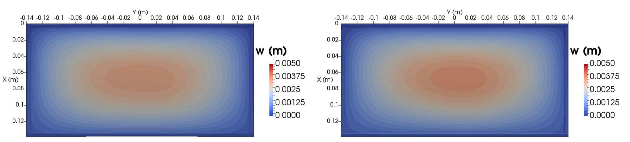

(c) $t^* = 16$. (d) $t^* = 20$.

Figure 10: Deformation contours for ~~$V = 8$~~$U_\infty = 8$ m/s, $\alpha = 8$ deg, membrane at 5.8% prestrain.

The primary wing deformation mode is an inflation that increases the local camber. A Proper Orthogonal Decomposition (POD) of the membrane deformation, for the problem with ~~$V = 8$~~$U_\infty = 8$ m/s, $\alpha = 8$ deg, with the membrane at 5.8% prestrain, shows that the main modes excited are the first four. They comprised about 85% of the original system energy, see Fig. 11(a) and Fig. 11(b).

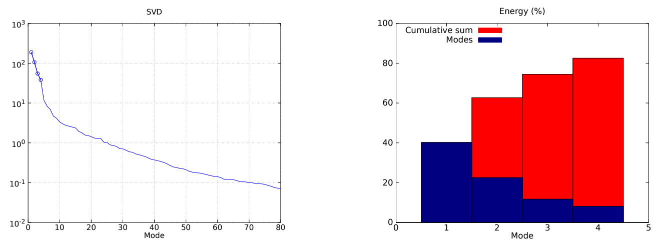

(a) SVD. (b) Energy content.

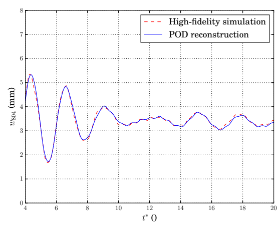

(c) POD reconstruction.

Figure 11: POD results for the flexible membrane at 5.8% prestrain, ~~$V = 8$~~$U_\infty = 8$ m/s, $\alpha = 8$ deg.

The first four Proper Orthogonal Modes (POMs) are shown in Fig. 12.

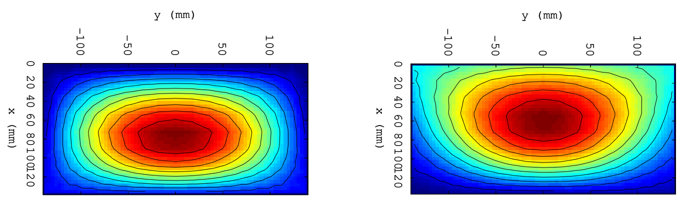

(a) POM 1. (b) POM 2.

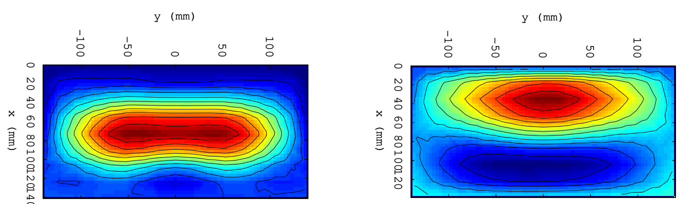

(c) POM 3. (d) POM 4.

Figure 12: First four POMs, ~~$V = 8$~~$U_\infty = 8$ m/s, $\alpha = 8$ deg, membrane at 5.8% prestrain.

In order to limit the ~~number~~ amount of data that has to be ~~post processed~~ post-processed for model reduction and allow ~~to~~ a preliminary assessment of the potentials of the POD for the aeroelastic problem of flexible membrane wings, only the structural degrees of freedom were considered in the POD. The coordinates of all the membrane points at every time step of the numerical simulation are used to build the snapshot matrix, $\mathbf{S}$, whose columns contain the values of the system variables at each time step. Afterwards, $\mathbf{S}$ is used for the calculation of the correlation matrix, $\mathbf{C} = \mathbf{S}^\top \mathbf{S}$. The eigenvectors of $\mathbf{C}$ define the basis of the projection matrix that can be used to project the time history of the state variables and obtain the time evolution of the amplitude of each base considered [57]. The amplitudes are the new variables of the ~~reduced order~~ reduced-order system; their number depends on the number of retained eigenvectors of $\mathbf{C}$. Fig. 11(c) compares the displacement history of the central point of the membrane from the ~~high fidelity~~ high-fidelity simulation and the POD reconstruction of the same time history with the 4 ~~modes selected~~ selected modes, and shows that the first four basis functions capture the displacement history well.

5.1.2. Effect on Flow Structure

Having established sufficient confidence in the aeroelastic membrane wing model, attention is now turned to the computed flow structures. No experimental validation is available for this work. Fig. 13 shows ~~a low pressure zone near wing tips, where~~ the predicted pressure contours by the coupled ~~fluid structure~~ fluid-structure simulation on the upper and the lower wing surface~~are plotted~~. The pres-

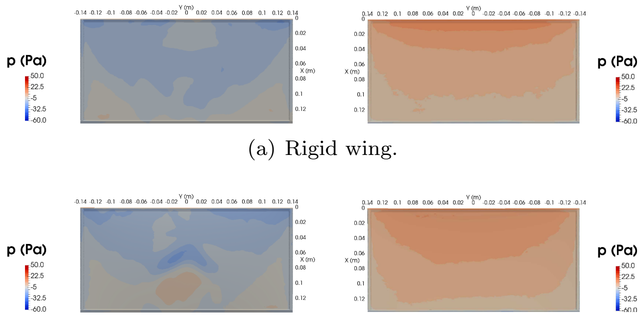

(a) Rigid wing.

(b) Membrane at 5.8% prestrain.

Figure 13: Pressure contours on the wing surface (Left: top, Right: bottom), ~~$V = 8$~~$U_\infty = 8$ m/s, $\alpha = 8$ deg, $t^* = 50$.

sure distributions at 8 deg angle of attack, ~~$V = 8$~~$U_\infty = 8$ m/s, for the upper surface of the rigid and flexible wing at 5.8% prestrain, are given in Fig. 13 (left). For the rigid wing, a high pressure region is located close to the leading edge, corresponding to flow stagnation. This is followed by pressure recovery (minimum pressure), and by a mild adverse pressure gradient, which is strong enough to cause the flow to separate. For the flexible membrane wing, the inflated membrane shape pushes the bulk of the flow separation closer to the leading edge. On the underside of the rigid wing, Fig. 13 (right), the pressure gradient is largely favorable, smoothly accelerating the flow from leading to trailing edge. Load alleviation on the lower surface of the flexible membrane wing is evident by a decrease in the ~~high pressure~~ high-pressure regions associated with camber, and a growth of the suction region at the trailing edge, presumably due to a decrease in the local incidence.

The pressure difference between the lower, ~~high pressure~~ high-pressure zone and the upper, ~~low pressure~~ low-pressure zone induces a spanwise flow that bends the streamlines towards the wingtips and accelerates the flow near the tips. The tip vortex can be easily observed from the streamline

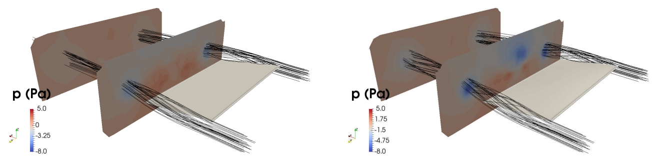

(a) Rigid wing. (b) Membrane at 5.8% prestrain.

Figure 14: Pressure contours and streamlines in the wake behind the wing, ~~$V = 8$~~$U_\infty = 8$ m/s, $\alpha = 8$ deg, $t^* = 50$; the cross-section planes are 0.5 c and 1.5 c behind the trailing edge.

structure. In Fig. 14 the pressure contours behind the rigid and the membrane wing at 5.8% prestrain are plotted, for R_e = 66k, at ~~$t^* = t\frac{V}{c} = 50$. The low pressure~~ $t^* = 50$. The low-pressure zone observed in the planes perpendicular to the flight direction characterizes the vortex core.

The effect of camber on flow structure is shown by the vorticity contours of Fig. 15, plotted at ~~$t^* = t\frac{V}{c} = 50$~~$t^* = 50$. The strongest wake vortices are located near the wing

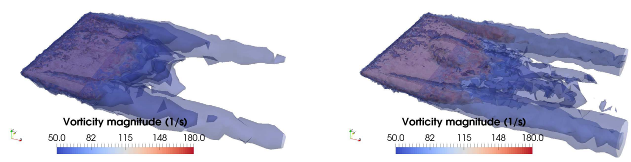

(a) Rigid wing. (b) Membrane at 5.8% prestrain.

Figure 15: Isosurface of vorticity, ~~$V = 8$~~$U_\infty = 8$ m/s, $\alpha = 8$ deg, $t^* = 50$.

tips, showing that the circulation gradient is largest there. Flow visualization suggests that the wing deformation contributes to stronger wing tip vortices.

5.2. Pitching Case

As demonstrated in previous results, both the unsteady numerical and the analytical static lift model adequately represent the lift behavior for the rigid and membrane wings within the study. This is important, since the (analytical) dynamic stall model is based on the static one, adding terms that account for pitch rates and time variant separation. Wings were tested under different flow velocities, $U_\infty = \{6, 8, 10\}$ m/s (i.e., $Re = \{50\text{k}, 66\text{k}, 84\text{k}\}$), two reduced frequencies, $k = \{0.05, 0.1\}$, and three AOA ranges, $\hat{\alpha} = \{0°$ to $10°$, $5°$ to $10°$, $10°$ to $20°\}$. The empirical time constant τ_2^* was tuned using dynamic wind tunnel data, cfr. [33], under low AOA pitching maneuvers[11]. Considering a single sinusoidal oscillation $\hat{\alpha}$ =

[11] For pitching maneuvers at low AOA, or where $X_{st}(\alpha) = 1$, the rate of trailing edge separation $\dot{X}_{st} = 0$, i.e., there is no separa-

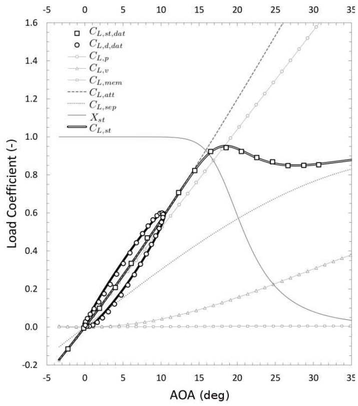

Figure 16: Dynamic lift model for rigid membrane, pitching at $k = 0.05$ for $\alpha_s = 0°$ and $\alpha_{amp} = 10°$, flow velocity of 8 m/s ($Re = 66k$).

$\{0°$ to $10°\}$, at a reduced frequency of $k = 0.05$, with a flow velocity of $U_\infty = 8\ m/s$ ($Re = 66$k), a value of $\tau_2^* = 4$ was found to produced accurate dynamic lift predictions, ~~both~~ as a function of α~~and time,~~ , as shown in Fig. ~~?? and ??, repectively.~~ 16. All subsequent results were computed with the same value of τ_2^*.

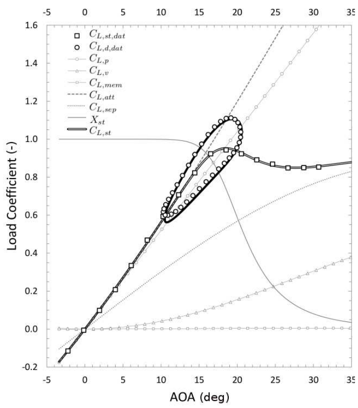

Figure 17: Dynamic lift model for rigid membrane, pitching at $k = 0.05$ for $\alpha_s = 10°$ and $\alpha_{amp} = 10°$, flow velocity of 8 m/s ($Re = 66k$).

Next, τ_1 was tuned using data from a high AOA sweep. Fig. 17 shows the same wing, with same flow conditions and pitch rate, but for a motion where $\hat{\alpha} = \{10°$ to $20°\}$. In this case, a value of $\tau_1 = 8.5$, produced accurate predictions with respect to AOA~~and time~~. This value of τ_1 was used for all the other ~~predicitons.~~ predictions.

With the established values for τ_1 and τ_2^*, all membrane wings subjected to all testing conditions could be modeled and compared to measured values. ~~For example, Fig. 19 shows the dynamic stall predicitonfor a membrane at 5.8% prestrain, with a flow velocity of 8 m/s~~Dynamic stall prediction for various membrane pretensions and flow velocities are reported in Fig. 18, 19, and 20. The results

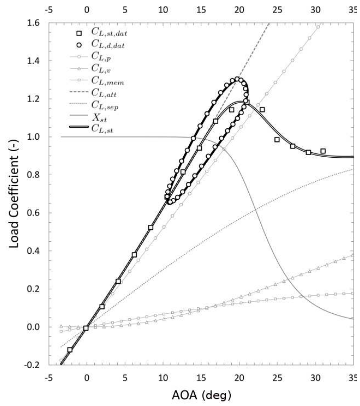

Figure 18: Dynamic lift model for a membrane at 8.5% prestrain, pitching at $k = 0.05$ for $\alpha_s = 10°$ and $\alpha_{amp} = 10°$, flow velocity of $10\ m/s$ ($Re = 84k$).

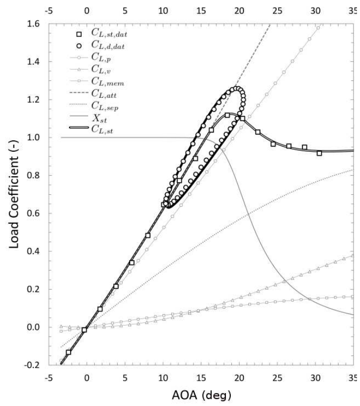

Figure 19: Dynamic lift model for a membrane at 5.8% prestrain, pitching at $k = 0.05$ for $\alpha_s = 10°$ and $\alpha_{amp} = 10°$, flow velocity of 8 m/s ($Re = 66k$).

produced by this predictive model appear to be fairly robust to changes in flow velocity, pitching frequency, AOA ranges, and membrane tensions.

6. Summary & Conclusion

A dynamic stall model is presented in this paper utilizing potential flow estimations of lift for static conditions to generate a static AOA lift model for attached and separated flow. Test data was used to predict the location of trailing edge separation for a given test scenario in order to produce an accurate static lift model for low to high AOA. This model incorporates a prediction of lift due to static leading edge flow separation and membrane cambering. The stability criteria for membrane cambering at zero AOA was identified, and the magnitude of unstable cambering was predicted with acceptable accuracy for the conditions tested. With a complete static lift model, dynamic variations of lift were included due to instantaneous flow recirculation effects, added mass effects, and transient flow separation. A ~~fist~~ first order, state space representation was used to model the time varying delayed separation

tion at low AOA. Thus, results are time invariant and are directly proportional to $\dot{\alpha}$, and $C_{L,d}$ is invariant to changes made to τ_1.

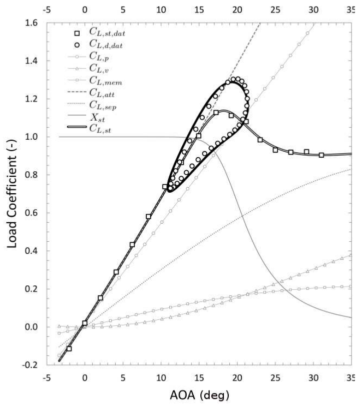

Figure 20: Dynamic lift model for a membrane at 2.0% prestrain, pitching at $k = 0.05$ for $\alpha_s = 10°$ and $\alpha_{amp} = 10°$, flow velocity of $6\ m/s$ ($Re = 50k$).

effect experienced at high AOA. Over a wide variety of flow conditions, pitching rates, AOA ranges, and membrane pretensions, the proposed analytical model produced acceptably accurate results.

A four–node four-node membrane element was implemented in a multibody–based co–simulation multibody-based co-simulation analysis for the direct simulation of coupled fluid–structure fluid-structure problems. As shown in the results, the numerical model accurately predicts attached flow conditions and trailing edge separation. Thus, it adequately represents the lift behavior for the membrane wings within this study. A methodology was also introduced for the reduced order modeling of the membrane wing based on proper orthogonal decomposition. POD projection allowed the definition of a very low order model that can capture the main features of the system, demonstrating the suitability of a reduction approach based only on structural information for the reduced–order reduced-order modeling of this class of aeroelastic systems.

This approach favorably correlated to data and could be well suited for real-time load estimation, given known airspeed and AOA. The concept of “feeling flight” is a simple one, yet the practical implementation and analytic formulation of this is not quite as straight forward. All told, this body of work has covered an array of load estimation approaches intended to further the understanding of the aerodynamics of membrane wings.

Acknowledgments

Effort sponsored by the Air Force Office of Scientific Research, Air Force Material Command, USAF, under grant number FA8655-12-1-2114, technical monitor Dr. Gregg Abate. The U.S. Government is authorized to reproduce and distribute reprints for Governmental purpose notwithstanding any copyright notation thereon.

[1] Y. Lian, W. Shyy, Three-Dimensional Fluid-Structure Interactions of a Membrane Wing for Micro Air Vehicle Applications, in: 44th AIAA/ASME/ASCE/AHS/ASC Structures, Structural Dynamics, and Materials Conference, American Institute of Aeronautics and Astronautics, 2003, dOI: 10.2514/6.2003-1726.
URL https://arc.aiaa.org/doi/abs/10.2514/6.2003-1726

[2] P. Ifju, M. Waszak, L. Jenkins, Stability and control properties of an aeroelastic fixed wing micro aerial vehicle, in: AIAA Atmospheric Flight Mechanics Conference and Exhibit, American Institute of Aeronautics and Astronautics, 2001, dOI: 10.2514/6.2001-4005.
URL https://arc.aiaa.org/doi/abs/10.2514/6.2001-4005

[3] R. Albertani, B. Stanford, J. P. Hubner, P. G. Ifju, Aerodynamic Coefficients and Deformation Measurements on Flexible Micro Air Vehicle Wings, Experimental Mechanics 47 (5) (2007) 625–635. doi:10.1007/s11340-006-9025-5.
URL https://link.springer.com/article/10.1007/s11340-006-9025-5

[4] R. Albertani, B. Stanford, J. Hubner, P. Ifju, Characterization of Flexible Wing MAVs: Aeroelastic and Propulsion Effects on Flying Qualities, in: AIAA Atmospheric Flight Mechanics Conference and Exhibit, American Institute of Aeronautics and Astronautics, 2005, dOI: 10.2514/6.2005-6324.
URL https://arc.aiaa.org/doi/abs/10.2514/6.2005-6324

[5] W. Shyy, H. Aono, S. K. Chimakurthi, P. Trizila, C.-K. Kang, C. E. S. Cesnik, H. Liu, Recent progress in flapping wing aerodynamics and aeroelasticity, Progress in Aerospace Sciences 46 (7) (2010) 284–327, doi:10.1016/j.paerosci.2010.01.001.

[6] A. Song, X. Tian, E. Israeli, R. Galvao, K. Bishop, S. Swartz, K. Breuer, Aeromechanics of Membrane Wings with Implications for Animal Flight, AIAA Journal 46 (8) (2008) 2096–2106. doi:10.2514/1.36694.
URL https://doi.org/10.2514/1.36694

[7] R. Waldman, A. Song, D. Riskin, S. Swartz, K. Breuer, Aerodynamic Behavior of Compliant Membranes as Related to Bat Flight, in: 38th Fluid Dynamics Conference and Exhibit, American Institute of Aeronautics and Astronautics, 2008, dOI: 10.2514/6.2008-3716.
URL https://arc.aiaa.org/doi/abs/10.2514/6.2008-3716

[8] P. Rojratsirikul, Z. Wang, I. Gursul, Unsteady Aerodynamics of Low Aspect Ratio Membrane Wings, in: 48th AIAA Aerospace Sciences Meeting Including the New Horizons Forum and Aerospace Exposition, American Institute of Aeronautics and Astronautics, 2010, dOI: 10.2514/6.2010-729.
URL https://arc.aiaa.org/doi/abs/10.2514/6.2010-729

[9] I. Gursul, D. J. Cleaver, Z. Wang, Control of low Reynolds number flows by means of fluid-structure interactions, Progress in Aerospace Sciences 64 (2014) 17–55. doi:10.1016/j.paerosci.2013.07.004.
URL http://www.sciencedirect.com/science/article/pii/S0376042113000857

[10] L. Ferguson, P. Seshaiyer, R. Gordnier, P. Attar, Computational modeling of coupled membrane-beam flexible wings for micro air vehicles, in: 48th AIAA/ASME/ASCE/AHS/ASC Structures, Structural Dynamics, and Materials Conference, American Institute of Aeronautics and Astronautics, 2007, dOI: 10.2514/6.2007-1787.
URL https://arc.aiaa.org/doi/abs/10.2514/6.2007-1787

[11] J. Babcock, R. Albertani, G. Abate, Experimental Estimation of the Rotary Damping Coefficients of a Pliant Wing, Journal of Aircraft 49 (2) (2012) 390–397. doi:10.2514/1.C031161.
URL https://doi.org/10.2514/1.C031161

[12] A. Song, K. Breuer, Dynamics of a Compliant Membrane as Related to Mammalian Flight, in: 45th AIAA Aerospace Sciences Meeting and Exhibit, American Institute of Aeronautics and Astronautics, 2007, dOI: 10.2514/6.2007-665.
URL https://arc.aiaa.org/doi/abs/10.2514/6.2007-665

[13] R. M. Waldman, K. S. Breuer, Shape, lift, and vibrations of highly compliant membrane wings, in: 43rd Fluid Dynamics Conference, American Institute of Aeronautics and Astronautics, 2013, dOI: 10.2514/6.2013-3177.
URL https://arc.aiaa.org/doi/abs/10.2514/6.2013-3177

[14] B. Stanford, P. Ifju, R. Albertani, W. Shyy, Fixed membrane wings for micro air vehicles: Experimental characterization, numerical modeling, and tailoring, Progress in Aerospace Sciences 44 (4) (2008) 258–294. doi:10.1016/j.paerosci.2008.03.001.
URL http://www.sciencedirect.com/science/article/pii/S0376042108000250

[15] O. M. Curet, A. Carrere, R. Waldman, K. S. Breuer, Aerodynamic Characterization of a Wing Membrane with Variable Compliance, AIAA Journal 52 (8) (2014) 1749–1756. doi:10.2514/1.J052688.
URL https://doi.org/10.2514/1.J052688

[16] W. McCroskey, L. Carr, K. McAlister, Dynamic stall experiments on oscillating airfoils, AIAA Journal 14 (1) (1976) 57–63. doi:10.2514/3.61332.
URL http://dx.doi.org/10.2514/3.61332

[17] L. W. Carr, Progress in analysis and prediction of dynamic stall, Journal of Aircraft 25 (1) (1988) 6–17. doi:10.2514/3.45534.
URL http://dx.doi.org/10.2514/3.45534

[18] F. Coton, R. Galbraith, Experimental study of dynamic stall on a finite wing, Aeronautical Journal 103 (1023) (1999) 229 – 236.

[19] G. Leishman, Dynamic stall experiments on the NACA 23012 aerofoil, Experiments in Fluids 9 (1990) 49–58.

[20] M. Goman, A. Khrabrov, State-space representation of aerodynamic characteristics of an aircraft at high angles of attack, Journal of Aircraft 31 (5) (1994) 1109–1115. doi:10.2514/3.46618.
URL http://dx.doi.org/10.2514/3.46618

[21] J. Larsen, S. Nielsen, S. Krenk, Dynamic stall model for wind turbine airfoils, Journal of Fluids and Structures 23 (7) (2007) 959 – 982. doi:http://dx.doi.org/10.1016/j.jfluidstructs.2007.02.005.
URL http://www.sciencedirect.com/science/article/pii/S0889974607000291

[22] W. McCroskey, The phenomenon of dynamic stall, in: Von Karman Inst. for Fluid Dynamics Unsteady Airloads and Aeroelastic Probl. in Separated and Transonic Flow, 1981.

[23] R. Cummings, S. Morton, S. Siegel, Numerical predictions and wind tunnel experiment for a pitching unmanned combat air vehicle, in: Aerospace Sciences Meetings, American Institute of Aeronautics and Astronautics, 2003, pp. –. doi:10.2514/6.2003-417.
URL http://dx.doi.org/10.2514/6.2003-417

[24] T. Beddoes, Onset of leading edge separation effects under dynamic conditions and low mach numbers, in: 34th Annual National Forum of the American Helicopter Society, American Helicopter Society, 1978.

[25] G. W. Reich, F. E. Eastep, A. Altman, R. Albertani, Transient Poststall Aerodynamic Modeling for Extreme Maneuvers in Micro Air Vehicles, Journal of Aircraft 48 (2) (2011) 403–411. doi:10.2514/1.C000278.
URL https://doi.org/10.2514/1.C000278

[26] N. Osterberg, Experimental Investigation of Dynamic Stall on Pliant Wings for Micro Air Vehicles, in: 54th AIAA Aerospace Sciences Meeting, American Institute of Aeronautics and Astronautics, 2016, dOI: 10.2514/6.2016-0146.
URL https://arc.aiaa.org/doi/abs/10.2514/6.2016-0146

[27] P. Masarati, M. Morandini, T. Solcia, A membrane element for micro-aerial vehicle fluid-structure interaction, in: P. Eberhard, P. Ziegler (Eds.), 2nd Joint International Conference on Multibody System Dynamics, Stuttgart, Germany, 2012.

[28] M. Alioli, Coupled fluid-structure simulation of flapping wings, Master's thesis, Politecnico di Milano (2011).
URL http://hdl.handle.net/10589/51142

[29] M. Alioli, M. Morandini, P. Masarati, T. Carpenter, R. Albertani, Nonlinear membrane inverse finite element model for pliant wings, in: SCITECH, Kissimmee, FL, 2015, AIAA2015-2051. doi:10.2514/6.2015-2051.

[30] M. Alioli, M. Morandini, P. Masarati, Coupled multibody-fluid dynamics simulation of flapping wings, in: ASME IDETC/CIE, Portland, OR, 2013, DETC2013-12198. doi:10.1115/DETC2013-12198.

[31] T. J. Carpenter, R. Albertani, Aerodynamic load estimation: Pressure distribution from virtual strain sensors for a pliant membrane wing, in: 54th AIAA/ASME/ASCE/AHS/ASC Structures, Structural Dynamics, and Materials Conference, 2013, doi:10.2514/6.2013-1917.

[32] E. C. Polhamus, A concept of the vortex lift of sharp-edge delta wings based on a leading-edge-suction analogy (nasa tn d-3767), Tech. rep., Langely Research Center, NASA (1966).

[33] T. J. Carpenter, Predicting Aerodynamic Loads on Highly Flexible Membrane Wings, Ph.D. thesis, Oregon State University (jun 2015).
URL http://hdl.handle.net/1957/56376

[34] J. Anderson, Introduction to Flight, 7th Edition, McGraw-Hill Education, New York, NY, 2011.

[35] E. C. Polhamus, A concept of the vortex lift of sharp-edge delta wings based on a leading-edge-suction analogy, Tech. Rep. NASA-TN-D-3767, NASA (Dec. 1966).
URL https://ntrs.nasa.gov/search.jsp?R=19670003842

[36] R. Sheldahl, P. Klimas, Aerodynamic characteristics of seven symmetrical airfoil sections through 180-degree angle of attach for use in aerodynamic analysis of vertical axis wind turbines, Tech. rep., Sandia National Laboratories (1981).

[37] P. Masarati, M. Morandini, P. Mantegazza, An efficient formulation for general-purpose multibody/multiphysics analysis, J. of Computational and Nonlinear Dynamics 9 (4) (2014) 041001, doi:10.1115/1.4025628.

[38] A. Logg, K.-A. Mardal, G. Wells (Eds.), Automated Solution of Differential Equations by the Finite Element Method, Vol. 84 of Lecture Notes in Computational Science and Engineering, Springer Berlin Heidelberg, Berlin, Heidelberg, 2012.

[39] J. C. Simo, M. S. Rifai, A class of mixed assumed strain methods and the method of incompatible modes, Intl. J. Num. Meth. Engng. 29 (8) (1990) 1595–1638, doi:10.1002/nme.1620290802.

[40] U. Andelfinger, E. Ramm, EAS-elements for two-dimensional, three-dimensional, plate and shell structures and their equivalence to HR-elements, Intl. J. Num. Meth. Engng. 36 (8) (1993) 1311–1337, doi:10.1002/nme.1620360805.

[41] J. Hoffman, C. Johnson, Computational Turbulent Incompressible Flow, Vol. 4 of Applied Mathematics: Body and Soul, Springer, 2007, doi:10.1007/978-3-540-46533-1.

[42] V. John, Slip with friction and penetration with resistance boundary conditions for the navier stokes equations - numerical tests and aspects of the implementation, Journal of Computational and Applied Mathematics 147 (2) (2002) 287–300, doi:10.1016/S0377-0427(02)00437-5.

[43] V. John, Slip with friction and penetration with resistance boundary conditions for the Navier Stokes equations - numerical tests and aspects of the implementation, Journal of Computational and Applied Mathematics 147 (2) (2002) 287–300, doi:10.1016/S0377-0427(02)00437-5.

[44] J. Hoffman, J. Jansson, R. Vilela De Abreu, Adaptive modeling of turbulent flow with residual based turbulent kinetic energy dissipation, Special Issue on Modeling Error Estimation and Adaptive Modeling 200 (3740) (2011) 2758–2767. doi:10.1016/j.cma.2010.11.016.
URL http://www.sciencedirect.com/science/article/pii/S0045782510003403

[45] G. Quaranta, P. Masarati, P. Mantegazza, A conservative meshfree approach for fluid structure interface problems, in: M. Papadrakakis, E. Onate, B. Schrefler (Eds.), Int. Conf. on Computational Methods for Coupled Problems in Science and Engineering, Coupled Problems 2005, CIMNE, Barcelona, 2005, Santorini, Greece, 2005.

[46] R. M. Waldman, K. S. Breuer, Shape, lift, and vibrations of highly compliant membrane wings, in: 43rd Fluid Dyn. Conf., San Diego, CA, United states, 2013, pp. American Institute of Aeronautics and Astronautics (AIAA) –.

[47] A. Pelletier, T. J. Mueller, Low reynolds number aerodynamics of low-aspect-ratio, thin/flat/cambered-plate wings, Journal of Aircraft 37 (5) (2000) 825–832. doi:10.2514/2.2676.

URL http://dx.doi.org/10.2514/2.2676

[48] A. Pelletier, T. J. Mueller, Low Reynolds number aerodynamics of low-aspect-ratio, thin/flat/cambered-plate wings, Journal of Aircraft 37 (5) (2000) 825–832. doi:10.2514/2.2676.
URL http://dx.doi.org/10.2514/2.2676

[49] W. Oswald, General formulas and charts for the calculation of airplane performance (naca-tr-408), Tech. rep., U.S. Department of Commerce, National Technical Information Service (1933).

[50] W. Oswald, General formulas and charts for the calculation of airplane performance (NACA-TR-408), Tech. rep., U.S. Department of Commerce, National Technical Information Service (1933).

[51] E. Lillberg, R. Kamakoti, W. Shyy, Computation of unsteady interaction between viscous flows and flexible structure with finite inertia, in: 38th Aerospace Sciences Meeting and Exhibit, American Institute of Aeronautics and Astronautics, 1999, dOI: 10.2514/6.2000-142.
URL https://arc.aiaa.org/doi/abs/10.2514/6.2000-142

[52] R. E. Gordnier, P. J. Attar, Impact of flexibility on the aerodynamics of an aspect ratio two membrane wing, Journal of Fluids and Structures 45 (2014) 138–152. doi:10.1016/j.jfluidstructs.2013.10.004.
URL http://www.sciencedirect.com/science/article/pii/S0889974613002235

[53] N. Osterberg, Experimental Investigation of Dynamic Stall on Pliant Wings for Micro Air Vehicles, in: 54th AIAA Aerospace Sciences Meeting, American Institute of Aeronautics and Astronautics, 2016, dOI: 10.2514/6.2016-0146.
URL https://arc.aiaa.org/doi/abs/10.2514/6.2016-0146

[54] R. Albertani, B. Stanford, P. Ifju, Unsteady Mechanical Aspects of Flexible Wings: Experimental Investigation of Biologically Inspired MAVs, in: MAV07 3rd US-European Competition and Workshop on MAV Systems & European Micro Air Vehicle Conference and Flight Competition 2007, ISAE-SUPAERO, Toulouse, France, 2007.
URL http://aeromav.free.fr/MAV07/session/plenary/SESSION%203/MAV07-PLEN%203-3%20Albertani/Albertani.pdf

[55] U. K. Chakravarty, R. Albertani, Experimental and Finite Element Modal Analysis of a Pliant Elastic Membrane for Micro Air Vehicles Applications, Journal of Applied Mechanics 79 (2) (2012) 021004–021004–6. doi:10.1115/1.4005569.
URL http://dx.doi.org/10.1115/1.4005569

[56] R. M. Waldman, K. S. Breuer, Shape, lift, and vibrations of highly compliant membrane wings, in: 43rd Fluid Dynamics Conference, American Institute of Aeronautics and Astronautics, dOI: 10.2514/6.2013-3177.
URL https://arc.aiaa.org/doi/abs/10.2514/6.2013-3177

[57] V. Buljak, Inverse analyses with model reduction: proper orthogonal decomposition in structural mechanics, Springer Science & Business Media, 2011.